NTNU

Norwegian University of
Science and Technology

Buckling of hollow rectangular aluminum columns

Vegard Nikolai Haraldseid

Master of Science in Mechanical Engineering
Submission date: June 2018
Supervisor: Magnus Langseth, KT
Co-supervisor: Marius Endre Andersen, KT

Norwegian University of Science and Technology
Department of Structural Engineering

Department of Structural Engineering
Faculty of Engineering
NTNU- Norwegian University of Science and Technology

ACCESSIBILITY

MASTER THESIS 2018

SUBJECT AREA:	DATE:	NO. OF PAGES:
Structural Engineering	11.06.2018	85

TITLE:

Buckling of hollow rectangular aluminum columns

Knekking av hule rektangulære aluminiumsøyler

BY:

Vegard Nikolai Haraldseid

SUMMARY:

This thesis is written at Structural Impact Laboratory (SIMLab) and the Centre of Advanced Structural Analysis (CASA) in collaboration with SINTEF and Statnett.

The capacity of simply supported aluminium columns exposed to both transverse loading and axial compression has been examined. The applicable column consists of an unsymmetrical cross section composed by a thin-walled hollow rectangle and a flange perpendicular to one of the major sides.

Tensile tests at the different section of the profile have been conducted. This, to detect eventual differences in the material properties and in the purpose to establish a constitutive stress-strain relation to be implemented in a numerical model. Both directions about the weak axis of the column were implemented in the experimental testing, and analytic and numerical analysis has been carried out and compared to the results.

Axial compression, which exposed the flange to tensional stresses, occurred in a local buckling mode that limited the columns capacity. By exposing the flange to compressional stresses, the column opposed bending propagation to a great extent.

RESPONSIBLE TEACHER: Professor Magnus Langseth

SUPERVISOR(S): Professor Magnus Langseth og Ph.D. Marius Endre Andresen

CARRIED OUT AT: The Department of Structural Engineering, NTNU

Institutt for konstruksjonsteknikk
Fakultet for ingeniørvitenskap
NTNU- Norges teknisk- naturvitenskapelige universitet

TILGJENGELIGHET

MASTEROPPGAVE 2018

FAGOMRÅDE:	DATO:	ANTALL SIDER:
Beregningsmekanikk	11.06.2018	85

TITTEL:

Knekking av hule rektangulære aluminiumsøyler

Buckling of hollow rectangular aluminum columns

UTFØRT AV:

Vegard Nikolai Haraldseid

SAMMENDRAG:

Denne avhandlingen er utført for Structural Impact Laboratory (SIMLab) og Centre of Advanced Structural Analysis (CASA) i sammarbeid med Statnett.

I studie har kapasiteten av hule aluminiums søyler utsatt for både transvers last og aksiell kompresjon blitt undersøket. Søylene har vært var innspent slik at de var fri til å rotere i begge ender. De er blitt utsatt for knekking i begge rettninger om den svake aksen. Tverrsnittet av søylen er usymmetrisk og består av en tynnvegget rektangulær del hvor den ene langsiden er påsatt en flens.

Strekktester fra ulike seksjoner i tverrsnittet av søylen er utført for å avsløre eventuelle forskjeller i material egenskaper, og for å etablere en konstitutiv spennings-tøynings relasjon for videre bruk i numerisk modellering. Det har blitt etablert analytiske og numersike løsninger for problemet som er blitt sammenlignet med de eksperimentelle dataene.

Ved å utsette søylen for aksiell kompresjon slik at tversnittet bøyes i en rettning som utsetter flensen for strekk spenninger oppstod det et lokalt kenkkingsmønster på trykksiden av søylen. Dette viste seg å begrense kapasiteten av søylen betraktelig. Ved å eksponere flensen for trykk absorberte søylen langt høyrer aksial krefter.

FAGLÆRER: Professor Magnus Langseth

VEILEDER(E): Professor Magnus Langseth og Ph.D. Marius Endre Andresen

UTFØRT VED: Institutt for konstruksjonsteknikk, NTNU

Institutt for konstruksjonsteknikk
FAKULTET FOR INGENIØRVITENSKAP OG TEKNOLOGI
NTNU – Norges teknisk-naturvitenskapelige universitet

MASTEROPPGAVE 2018

For Vegard Haraldseid

Knekking av hule rektangulære aluminiumsøyler

Buckling of hollow rectangular aluminum columns

Statnett ønsker å vurdere bruk av aluminium som konstruksjonsmateriale i høyspentmaster. Enkle beregninger basert på EC9 indikerer en totalvekt på ca. 5500 kg for en aluminiummast sammenlignet med 9100 kg for en tilsvarende mast i stål. Foreløpige vurderinger indikerer at denne vektbesparelsen ikke gir tilstrekkelig kostnadsbesparelse til at dette er et interessant prosjekt for Statnett. Dette synliggjør behovet for mere nøyaktige verktøy hvor en optimal kombinasjon av material og geometri kan etableres. Avanserte FEM beregninger tilpasset aluminium som konstruksjonsmateriale kan være et alternativ for å få en tilfredsstillende vektbesparelse.

Denne oppgaven er en del av dette prosjektet. Målet med oppgaven er å etablere validerte numeriske analysemodeller for et gitt søyleprofil i aluminium. Søyleprofilet er et tynnvegget rektangulært profil med en ekstern flens på en side. Denne profilgeometrien kan føre til interaksjon mellom lokal og global knekking, og en søyle i dette profilet vil oppføre seg forskjellig etter hvilken side som havner i trykk. Dette skal undersøkes med numeriske analysene skal valideres mot utførte forsøk og vurderes opp mot beregninger etter EC9. Følgende foreløpige plan er definert for denne oppgaven:

- Det skal gjennomføres et litteraturstudium knyttet til oppførsel og modellering av søyler i aluminium utsatt for aksiallast.
- Kandidaten skal delta i planlegging og gjennomføring av materialforsøk på en 6082-T6 legering. Materialforsøkene skal brukes til å evaluere variasjonen av materialegenskaper rundt i profilet.
- Kandidaten skal delta i planlegging og gjennomføring av knekkingsforsøk. Det skal etableres en forsøksrutine for å gi konsistente resultater.
- Det skal etableres numerisk modeller for global knekking som skal valideres mot de testene som er utført.
- Resultater fra forsøk og numeriske beregninger skal sammenlignes med beregninger etter EC9.
- Rapportering.

Veiledere: Magnus Langseth og Marius Andersen

Kandidaten kan fravike den foreslåtte plan, men kun etter avtale med veilederne. Hovedoppgaven skal skrives på engelsk og utformes som en forskningsrapport og i henhold til gjeldende regler for en hovedoppgave. Oppgaven skal leveres til Institutt for konstruksjonsteknikk, NTNU innen 11. juni 2018.

Acknowledgments

This thesis was compiled for the Structural Impact Laboratory (SIMLab) and the Centre of Advanced Structural Analysis (CASA) in collaboration with Statnett at the Department of Structural Engineering at the Norwegian University of Science and Technology (NTNU). An initiative by SINTEF and Statnett developed into a project named: -"Design of power pylons in aluminium customized for automatic production". By studying the capacity of a hollow aluminium profile, this thesis will contribute to the program, supervised by Professor Magnus Langseth and Ph.D. Marius Endre Andersen.

The enthusiasm and transparency of Marius Endre Andersen have made this thesis what it is. I would like the thank him for much-appreciated discussions and guidance throughout the semester.

Magnus Langseth's supervision regarding the experimental work and analytical in addition to numerical problem solving has been valuable in the compilation of this thesis. The analytical solutions in these theses could not have been conducted without him and is highly appreciated.

I would like to thank Maria-Monika Metallinou Log for a extraordinary, comprehensive and constructive feedback on the complete thesis.

The IT-support that Asle Skauge has to provide has by far simplified the process in this thesis. I would like to thank him for his collaboration.

With supervision regarding the digital image correlation software eCorr, the developer Egil Fagerholdt has been essential.

I would especially like to thank co-students Benjamin Stavnar Elveli, Mads Bakken Iddberg, Christoffer Martinsen, Nikolai Korvald Skaar and Jone Nicolai Sigmundstad countless discussions, feedback, and support through the compilation of this thesis.

One last gratitude belongs to Martin Hals, Kristine Haraldseid, Cecile Haraldseid, Therese Haraldseid and Gunn Haraldseid.

Trondheim, 11.06.2018

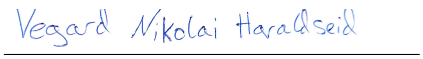

Vegard Nikolai Haraldseid

Abstract

This thesis contributes a project initiated by SINTEF: "Design of power pylons in aluminium customized for automatic production", in conjunction with Statnett and CASA. Through laboratory work, the capacity of a simply supported aluminium column was examined. The column holds a hollow rectangular cross-section with a flange perpendicular to one of the major sides. Different tests have been conducted where the column was bent both ways about the weak axis exposing the flange for either tensional or compressional stress. The experimental results have been compared to analytical solutions in addition to numerical analysis.

Tensile tests were conducted to achieve material properties to be implemented in the numerical model and in order to detect eventual different material properties at different sections of the profile. The raw data were analyzed with DIC, post-processed through Python and validated by numerical analysis in Abaqus. A constitutive stress-strain relation was established and reaffirmed before implemented into the numerical model of the column.

The major finding occurred by exposing the flange of the column to tensional stresses. These series of tests resulted in a repetitive local buckling pattern at the compressional side of the profile moments before the column achieved its maximum capacity. By comparing the experimental data to analytical solution, it becomes clear that the local buckling limits the capacity of these series.

For the analytical solutions, a theoretical approach by far described the bending propagation. Calculations based on Eurocode 9 underestimated the columns capacity. The highest deviation was found to be surprisingly high as it reached values of nearly 25 % short.

The numerical analysis was run implicit and did struggle to converge. Despite this, accurate solutions were successfully established.

Sammendrag

Denne avhandlingen er et bidrag til Statnett sitt prosjekt med tittelen: "Design av aluminiumsmast tilpasset automatisert produksjon". Fokuset i denne oppgaven er rettet mot en 2.5 meter lang søyle utsatt for både aksial kompresjon og en transvers last. Søylen er fri til å rotere i begge opplager og består av et usymmetrisk tverrsnitt, noe som kompliserer problemet. Tverrsnitte er bestående av et rektangulært profil med en flens påsatt en av langsidene.

Det har blitt gjennomført i alt 8 eksperimentelle tester hvor søylen ble lastet både slik at flensen ble trykksatt, og slik at flensen ble utsatt for strekk. I tillegg var den transverse lasten påsatt med forskjelig kraft. Videre har de experimentelle datane blitt sammenlignet med både analytiske løsninger og numeriske analyser.

Det har blitt utført flere strekktester med det formål å kunne konstatere eventuelle variasjoner av materialegenskaper i forskjellige seksjoner av tverrsnittet. I tillegg var det et mål å etablere konstitutive spenning-tøynings relasjoner som kunne brukes i den numersike modelleringen.

Et oppsiktsvekkende resultat viste seg å oppstå for testene hvor en utsatte flensen for strekktøyninger. Dette viste seg å føre til et lokalt repetativt knekkingsmønster på trykksiden av søylen. Ved å sammneligne eksprimentelle verdier med de analytiske veridene ble det klart at den lokale knekkingen satt en klar begrensning for kapasiteten til søylen.

For søylene som ble testet ved å eksponere flensen for trykk var en av hypotesene at denne flensen hadde en så stor slankhet at den ville oppnå en lokal knekking for så å trigge en global knekking for hele søylen. Det viste seg tvert imot at flensen motsatte seg lokal knekking opp til svært høye forskyvninger, og at den først oppstod for forskyvninger langt høyere enn for de forskyvningene der den globale knekkingen inntraff. Når det kom til den teoretiske tverrsnittskapasiteten som er begrenset av flytspenningen i materialet så viste det seg at denne underestimerte den faktiske kapasiteten av søylen.

For de implisitte numeriske analysene så viste det seg at det skulle bli vanskelig for løsningen å konvergere for testene hvor det lokale bucklingsmønsteret oppstod.

Dette er koblet med at det oppstår en høy geometrisk ikkelinearitet i analysen noe som en implisitt analyse vil ha vanskeligheter med å representere. I tillegg er det vanskelig å oppnå lokal knekking når en driver med numeriske analyser hvor både geometri og materialet er homogent og uten defekter, dette siden knekkning er et ustabilitets problem som vil trenge en ujevnhet for å igangsette. Det ble likevel gjennomført analyser som inneholdt høy presisjon sammenlignet med til de eksperimentelle verdiene.

For de resterende testene hvor flensen oppnådde kompresjonsspenninger så tenderte den numeriske analysen i en konservativ rettning. For en av testene underestimerte analysen de experimentelle verdiene med 6 %

Contents

List of Figures

List of Tables

Abbreviations and nomenclature

Abbreviations

2D	Two dimensional
App.	Appendix
CAD	Computer Aided Engineering
CASA	Centre for Advanced Structural Analysis
CPU	Central prepossessing unit
DIC	Digital Image Correlation
EC9	Eurocode 9: Design of Aluminium Structures, Part 1-1
Eq.	Equation
FEA	Finite Element Analysis
FEM	Finite Element Method
Fig.	Figure
FT	Flange in tension
NTNU	University for Science and Technology
Sec.	Section
SIMLab	Structural Impact Laboratory

Nomenclature

A	Cross sectional area
A_{eff}	Effective area, EC9
A_0	Initial cross sectional area
C_n	Voce rule parameter
C_p	Plastic neutral axis
C_y	Neutral y-axis
C_t	Neutral axis in transition
C_{0y}	Neutral y-axis for rectangular section
Δ_N	Difference between buckling load, experimental data
ds	Infinite length of curvature
dx	Infinite length of curvature
E	Young's modulus
h	Height of gauge area in tensile test specimen
I	Second area of momentum
L	Length of column
L_B	Buckling length
L_1	Distance to the rotational center

L_0	Initial column length
M	Momentum
$M_{y,Ed}$	Is the bending moment about the y-axis, EC9
$M_{y,Rd}$	Is the bending moment capacity about the y-axis, EC9
N	Axial load
N_B	Buckling load
$N_{b,Rd}$	Design buckling resistance of compression member, EC9
N_{Cr}	Critical load
N_{Ed}	Design value of compression force, EC9
$N_{El.Cap}$	Elastic capacity load.
N_E	Eulers critical load
p	Equivalent plastic strain
Q_n	Voce rule parameter
$R(p)$	Hardening law
R	Radius
r	Radius of gyration
w	Width of gauge area in tensile test specimen
W_y	Elastic resistance

Greek symbols

α_B	Angle bottom support
α	Angle supports
α_T	Angle top support
β	Parameter, local buckling, EC9
χ	Parameter, local buckling, EC9
ω	Deflection
δ	Mid span deflection
$\overline{\lambda}$	Relative slenderness
Δ_δ	Difference between mid span deflection, experimental data
$d\phi$	Infinite angle of curvature
ϵ	Strain
ϵ_{EC9}	Parameter, local buckling, EC9
$\epsilon_{\delta,max}$	Strain at maximum transverse mid span displacement
ϵ^e	Elastic strain
ϵ_e	Engineering strain
ϵ_0	Initial strain
$\epsilon_{N,max}$	Strain at maximum axial load
ϵ^p	Plastic strain
ϵ	True strain
κ	Safety factor for weakening effects of welds, EC9
γ_1	Safety factor decided by national annex, EC9
ν	Poisson's ratio
$\omega_{0,EC9}$	Is a factor that includes weakening effects due to welding and holes, EC9
ω_0	Deflection initial
ρ	Density
σ	Stress
σ_e	Engineering stress
σ_E	Eulers critical Stress
σ_0	Yield stress
σ	True stress
λ	Slenderness ratio

Chapter 1

Introduction

1.1 Background

Statnett is the responsible administrator of the Norwegian electrical high voltage grid, which implies operation and maintenance control of 11 000 km of power pylons [1]. It is forecasted that 1000 new power pylons per year will be required in the period 2015-2025. A cost-efficient design is therefore highly requested. SINTEF has in a collaboration with CASA and other relevant companies within the industry initiated a project: "Design of power pylons in aluminium customized for automatic production" [2]. Due to the long distances and demanding geography in the Norwegian backcountry, several of the assemblies need to be transported by helicopter. A cost-efficient design will, therefore, consist off a cheap production process in addition to a lightweight geometry which is easily transportable. Aluminium is of interest due to its high strength and light weighted characteristics [3]. In addition to aluminium's high ductility, it is possible to extrude a design which could be a major advantage if this feature is utilized properly. It is on the other hand, both energy demanding and costly to produce and extrude aluminium. A light weighted construction is therefore essential to justify this choice of material.

A power pylon in aluminium, based on the Eurocode 9 has been produced, where a weight reduction of 40 % has been achieved [4]. A detailed study, determining the exact capacity of each loadbearing member, is necessary to further reduce weight and deviate from yielding standards. Through precise experiments and numerical analysis, this thesis will describe a specific slender aluminium column exposed to axial loading. Analytical solutions, both based on a theoretical approach and the Eurocode 9 [5], will be compared to the experimental findings. These results are one step in the design of a power pylon in aluminium.

1.2 Study

The profile studied in this thesis holds a hollow rectangular cross-section with rounded edges and a flange that stands perpendicular to one of the major sides. The profile is presented with dimensions in Fig. 1.1. Twelve tensile tests were performed in an attempt to detect different material properties at different sections of the profile. DIC analysis was conducted to retrieve elongation of the specimens. The raw data were post-processed in python for material calibration, further to be implemented in a numerical model.

In total were eight different columns of length 2.5 m exposed to both axial loading and a constant mid-span transverse load. The different tests were divided into two main groups where the flange was exposed to either tensional or compressional stresses. In addition were these two main group divided into two subgroups each, where a transverse mid-span load of either 200 kg or 100 kg was applied.

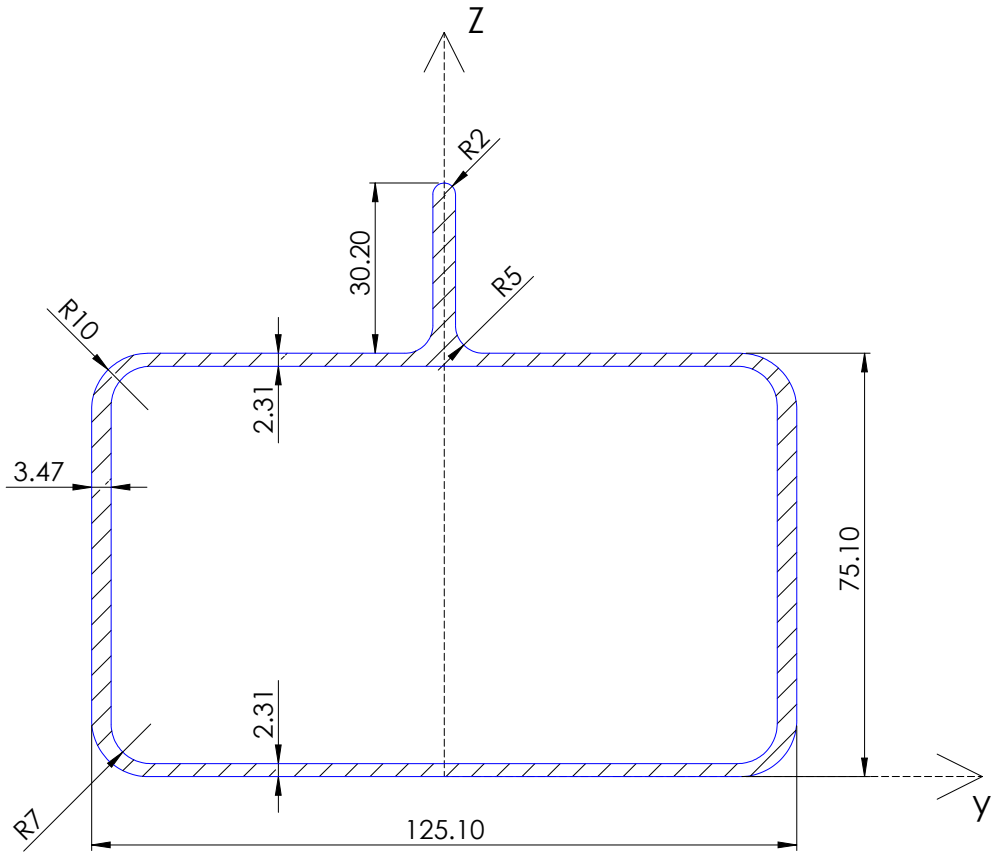

Figure 1.1: Profile dimensions. All measures in mm.

The flange will be used to attach ladder steps in the power pylons and contributes to a rather complex problem creating an asymmetrical cross-section. It will behave as a strut to the symmetrical rectangular profile. Different behavior is expected by exposing the flange to compressional or tensional stresses. Analytic calculations from a theoretical approach and EC9 have been established. In addition, has

numerical analysis been conducted. These will be compared to the experimental results.

The cross-section of the column is illustrated in Fig. 5.1 Ch. 5 together with the specifications listed in Tab. 5.1. An implication of adding a flange to a symmetrical rectangular cross section is the translation of the neutral axis. The column will be exposed to bending in both directions about the weak axis. Especially two phenomena are of interest. While bending the column as the flange is exposed to tension the major side of the profile is expected to achieve high compressible stresses which will force it into an unstable region. The same accounts for an axial loading that exposes the flange to compression, however, the unstable part is then predicted to be the flange itself.

1.3 Previous studies

No data were found in the literature regarding the particular problem examined in the present thesis. There was not any success in obtaining a study that does address the specific column this thesis does examine. However, there has been completed three master thesis at SIMLab and CASA motivated to SINTEF's initiative by power pylon design in aluminium.

The behavior of circular cylinders exposed to axial load and transverse mid-span load where studied by Nesje and Nilsen [6]. This work was continued by Amundsen and Lynum [7]. Welded circular cylinders exposed to axial compression were studied by Guddal [4]. These three theses were relevant in the process of developing a theoretical background and the establishment of the laboratory setup for the experimental testing conducted in the this tehsis.

For the material properties, there has been evaluated a Voce hardening rule to the 6082 T-6 alloy which is the material utilized in this study. This work was developed by Hopperstad et al. [8]. Material calibrations of 6082-T6 alloy have also been conducted in the thesis by both Nesje and Nilsen [6], and Amundsen and Lynum. [7].

Clausen, Hopperstad, and Langseth examined stretch bending of aluminium extrusions for rather complex geometries for alloys in the 7000-series [9]. In addition, there has been conducted studies by Paulsen and Welo on bending of rectangular hollow aluminium sections of 6060 alloys [10]. Both these studies are targeting the car industry.

1.4 Outline of the Study

Ch. 2. Theory: Presentation of theoretical assumptions and calculations relevant to the study. This includes material behavior and mechanics, buckling theory

and analytical approaches.

Ch. 3. Material calibration: Experimental tensile testing, analyzed through DIC are to be presented. The raw data are post-processed through python to establish a constitutive stress-strain relation. Numerical implementation was conducted for validation.

Ch. 4. Laboratory: Practical implementation of the laboratory setup and measurements will be presented.

Ch. 5. Laboratory experiments: Information about the column studied in this thesis including cross-sectional properties will be given. The experimental results will be presented and discussed.

Ch. 6. Analytic approach: Analytical results based on theoretical assumptions and EC9 will be compared to the experimental results.

Ch. 7. Numerical approach: Presentation of the numerical model and analysis. Results of the numerical analysis compared to the experimental results.

Ch. 8. Accuracy and precision: Discussion on the reliability of the experimental implementation and numerical model and analysis.

Ch. 9. Conclusion: Outlining of the essential findings of the study.

Ch. 10. Further work: Outlining of further topics of interest that could be relevant for future work, based on the findings of the study conducted.

1.5 Software

Abaqus FEA: Abaqus FEA was in this study utilized to run numerical analysis based on the finite element method FEM [11].

Autodesk Robot: Autodesk Robot is a structural analysis program, in this study used to establish cross-sectional properties [12].

eCorr: eCorr is a digital image correlation program and was used in this study to examine experimental tensile testing [13].

Gimp: Gimp is an image manipulation program. It was used to manipulate pictures for illustrative purposes [14].

Python: Python is an object-orientated, high-level programming language. Data processing, graphs, and illustrations were established through Python [15].

Solidworks: Solidworks is a computer-aided design program (CAD) used for illustrative purposes in this study [16].

Latex: This thesis was written utilizing the documentation preparation system Latex [17].

Chapter 2

Theory

2.1 Material

The material applied in this study is an aluminium alloy of type 6082-T6. Aluminium is produced in many alloy compositions and is in general known to possess properties as high strength, low weight, and high ductility. Aluminium is produced through refining oxide from bauxite and process it through electrolysis. In its purest form it is soft and ductile. Different material properties are assigned through alloys and heat treatment. The first of the four digits in the alloy description indicates which series the alloy is representing. The second assigns if there are any variations in the alloy. The two last digits state the composition of the elements in the alloy. The first number, in the 6082-T6 alloy, indicates that this is an alloy within the 6000 series, consisting of the main elements aluminium, magnesium, and silicone. This series is characterized by versatile, moderately high strength, corrosion resistance, and weldable abilities. The second number, 0, indicates that there should not be any variation of the composition in the alloy. The third and fourth number indicates the amount of magnesium and silicone in the alloy [3].

The T6 labeling indicates solution heat treatment and artificially aging. This process consists of heating the alloy to nearly melting temperature before quenching it to room temperature. This results in a solution with high internal stresses resulting in a high strength but in addition brittle material properties. To reduce the brittle behavior, and increase ductility, the alloy is artificially aged. This will reduce the amount of internal stresses, lower the strength and increase the ductility of the alloy [18]. For more comprehensive reading it is referred to Aluminum.org [3], Kaufman [19] and Anderson [18].

Further, this material has been extruded which also affects the material properties. This will be discussed in Sec. 2.2.

2.2 Extrusion

Extrusion is a common method for processing aluminium stating as a solid bar, to achiev a complex fixed cross-section. Extrusion is known to be accurate in the longitudinal direction, however, there could be some minor deviation in the transverse direction of the column. This can be caused by a rough surface, or if the extrusion objects are not aligned properly. The quality of an extruded aluminium profile is highly dependent on the accuracy during the process, and therefore the manufacturer [20].

Aluminium is mostly extruded using a hot direct process where the raw material is heated to 450 ^{o}C to 580 ^{o}C and forced through a die to form cross-sectional properties [21]. This process affects the microstructure of the aluminium, resulting in some implications. Heat treatment will be an implicit result of the extrusion process. This heat treatment will vary with the cross-sectional thickness and result in different material properties for cross-sections with varying thickness. Twelve tensile tests were performed in this study, in order to retrieve material properties and to investigate the potential differences related to the varying thickness at different regions.

Age hardening, which is more correctly referred to as participation hardening, is a method that's is used to reduce dislocations in the lattice of a material. Dislocations and plasticity are tightly coupled since plastic strains do occur by moving dislocations permanently in the lattice illustrated in Fig. 2.1. A perfect lattice will, by definition of plastic strains, only experience elastic strains. Materials will never obtain a perfect lattice. However by reducing dislocations an increase of the yield strength will occur, as described by Anderson [18].

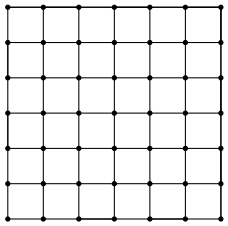

(a) Perfect lattice, will in theory only retrieve elastic strains.

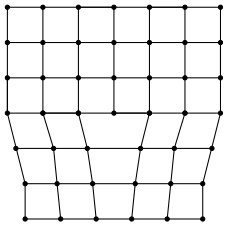

(b) Dislocation in the lattice.

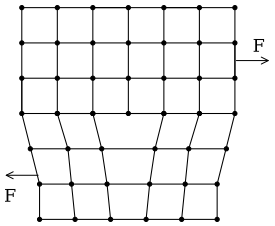

(c) Force applied to the material component.

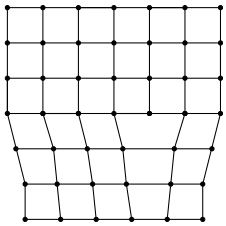

(d) Change of dislocation in lattice, plastic deformation occur.

Figure 2.1: Material lattice.

2.3 Stress-strain relations

Tensile tests were conducted in order to obtain a constitutive stress-strain relation for the column at hand. The experimental testing retrieves the elongation of the specimen as well as the force applied in multiple numbers of frames. To post process this information into Abaqus it is be necessary to derive a constitutive stress-elastic strain as well as a stress-plastic strain relation as the total strain is defined by Eq. 2.1. Expressions are found utilizing the work of Hopperstadt and Børvik [22], which is referred to for more comprehensive reading on the subject.

$$\epsilon = \epsilon^e + \epsilon^p \tag{2.1}$$

From the cross-sectional area and the applied force, it is possible to obtain the engineering stress σ_e, defined in Eq. 2.2.

$$\sigma_e = \frac{N}{A_0} \tag{2.2}$$

The elongation of the dog bone specimen is by definition equal to the engineering strain ϵ_e. The true strain ϵ is given as a logarithm where the engineering strains are included in Eq. 2.3. Hooke's law will be utilized in order to define a constitutive stress-strain relation for the elastic region of the strain evolution, and is presented in Eq. 2.4.

$$\epsilon = ln(1 + \epsilon_e) \qquad (2.3) \qquad\qquad \sigma = E\epsilon \qquad (2.4)$$

The true stress is given in Eq. 2.5. Both the true strain and true stress are derived in App. A.

$$\sigma = \sigma_e(1 + \epsilon_e) \qquad (2.5)$$

A constitutive stress-plastic strain relation is further to be presented by the yield stress and the hardening law of the material Eq. 2.6. When dealing with aluminium it is recommended to use the Voce rule, Eq. 2.7 to describe the hardening propagation. Voce hardening is a summation rule, defined by the parameters Q and C and the equivalent plastic strain p.

$$\sigma = \sigma_0 + R(p) \qquad (2.6) \qquad R(p) = \sum_{n=1}^{\infty} Q_n(1 - e^{-C_{np}}) \qquad (2.7)$$

2.4 Buckling

Buckling is an instability problem and can occur in columns as a local mode or a global mode, highly dependent on slenderness. Slenderness describes either the ratio between the length and the cross-section of a column, column slenderness, or the wall thickness to length ratio of the cross-section, cross-sectional slenderness. There is not any exact distinction between when a local or a global buckling mode occur. There is also a possibility that they can occur at the same time. However, certain columns are prone to one or the other mode while exposed to axial compression. A local buckling mode is likely to occur in thin-walled members where the cross-sectional slenderness is high as in Fig. 2.2a. A global buckling mode is, on the other hand, more likely to occur in columns where the column slenderness ratio is high as in Fig. 2.2b.

Buckling is an instability problem. A stable system will always return to a position of equilibrium. An unstable system could, however, continue into a non-equilibrium path when exposed to relatively small disturbances. There are three terms that are of especially interest when it comes to the deformation of a slen-

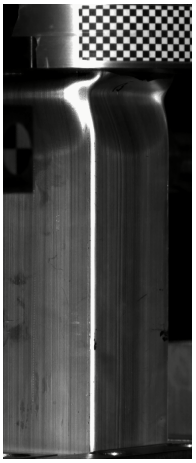

(a) Local buckling mode.

(b) Global buckling mode.

Figure 2.2: Buckling modes.

der column due to axial compression. That is primary path, secondary path, and bifurcation point, illustrated in Fig. 2.3b. A primary path is where a small increase in applied load is met by an equivalent small response. A secondary path is when the response is significant compared to the applied load to the system. The bifurcation point is the point of instability where the two paths meet.

By considering the 2D elastic column exposed to an increasing axial compression in Fig. 2.3a, there are two possible outcomes. The column will at some point retrieve an unstable condition i.e a bifurcation point. The bifurcation is the point where the two possible outcomes meet. The primary path is where the column counteracts the axial load by internal elastic stresses. The secondary path is where the column will enter a global buckling mode and counteract the axial load by a bending moment. This bending moment is defined in Eq. 2.9. To exhibit a moment that is sufficiently large to meet the axial load a significant increase in deflection will occur. This is the definition of the secondary path, i.e. the point where the internal forces are transferred from stresses into bending moment. The theory in this section is retrieved from Cook et al. [23] and Larsen [24], which is referred to for more comprehensive reading on the subject.

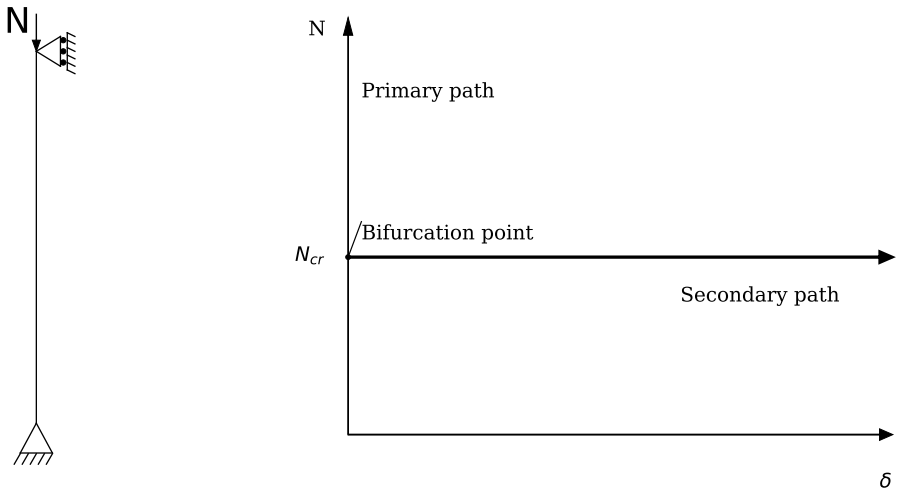

(a) A slender column exposed to axial compression.

(b) Important definitions of buckling.

Figure 2.3: Buckling theory.

2.5 Analytic solutions

The present thesis focuses on two analytical approaches. Euler's critical load, based on the assumption of elastic global buckling, and cross-sectional capacity, limited by the yielding of the material, are the theoretical approach. The second approach is based on the Eurocodes obtained from Eurocode 9, from now on referred to as EC9. Information on these topics are retrieved partialy from Larsen [24] and EC9 [5].

2.5.1 Theoretical approach

Euler's critical load

All calculations in this section are found in Larsen [24]. Euler's critical load was developed by the Swiss mathematician Leonhard Euler in 1757 [25]. Based on the Euler-Bernoulli beam theory where the deflection of a beam exposed to axial loading is to be described by a simple sinus curvature given in Eq. 2.8 and illustrated in Fig. 2.4a. Given the deflection of the column, the momentum can be described as in Eq. 2.9. Based on this momentum equilibrium equation and the assumption of curvature, Euler developed his theory on critical loading on slender columns based on the following assumptions:

- The column is straight and without any imperfections
- The material is elastic and obeys Hooke's law

- The load is applied at the centroid of the cross section
- The column deflection is small compared to its length

$$\omega = \delta Sin(\frac{\pi x}{L}) \qquad (2.8) \qquad\qquad M = N\omega \qquad (2.9)$$

In beam theory, the deflection is assumed to be small compared to the length. Based on that assumption it is reasonable to state that the length of the curvature is approximately the length over an infinitesimal. In other words $ds \approx dx$ in Fig. 2.4b. This assumption is the reason why the Euler critical load is known as a linearized approach. Further, the curvature can be derived as in Eq. 2.10. By assuming small deflections the curvature could be defined as in Eq. 2.11 by considering the cross-sectional area in Fig. 2.4c.

$$\frac{1}{R} = \frac{d\phi}{ds} \approx \frac{d\phi}{dx} \approx \frac{d}{dx}\frac{d\omega}{dx} = \frac{d^2\omega}{dx^2} \qquad (2.10)$$

$$\frac{1}{R} = \frac{\epsilon}{H/2} \qquad (2.11)$$

By implementing Hooke's law and moment equilibrium, Eq. 2.12 can be obtained. Further, the terms can be rearranged and solved for the momentum, Eq. 2.13, where the expression for curvature is implemented from the linearized expression, Eq. 2.10. The minus sign in front of Eq. 2.13 is due to the definition of positive momentum.

$$\frac{R}{E}\cancel{H/2} = \frac{M}{I}\cancel{H/2} \qquad (2.12) \qquad\qquad M = -EI\frac{d^2\omega}{dx^2} \qquad (2.13)$$

Finally, by differentiating the deflection in Eq. 2.8 and the equation of moment equilibrium in Eq. 2.9 into Eq. 2.13, Eulers critical load can be obtained in Eq. 2.14.

$$\boxed{N_E = \frac{\pi^2 EI}{{L_B}^2}} \qquad (2.14)$$

Euler's critical load can be used to calculate the buckling load of all kinds of slender columns regardless of the cross-sectional area and boundary conditions as well as global buckling modes. This study will focus on simply supported columns of a first order buckling mode, which results in a reduction factor of 1 giving buckling length L_b equal to the actual length L of the column.

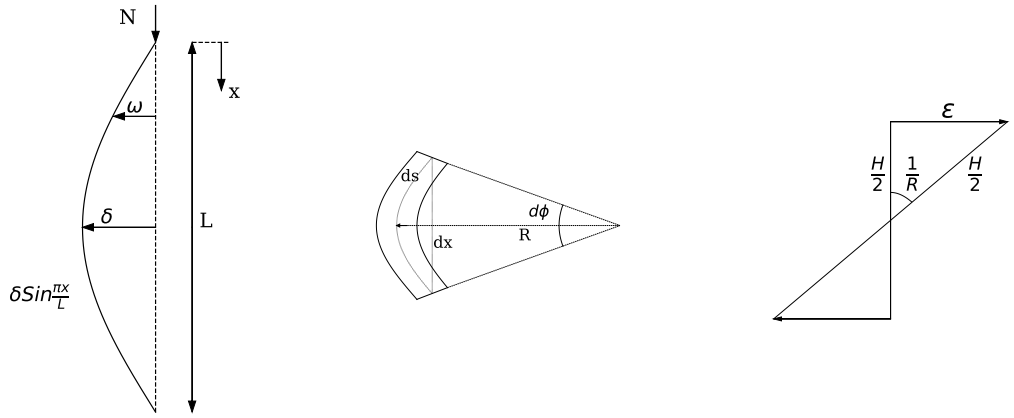

(a) Assumed deflection of a simple supported column exposed to axial compression.

(b) Curvature element in column.

(c) Strain distribution over the element.

Figure 2.4: Beam theory.

The slenderness ratio of a column is defined in Eq. 2.15 where r is the least radius of gyration. Further based on the second order of momentum calculated about the weak axis of the cross-section, defined in Eq. 2.16.

$$\lambda = \frac{L}{r} \qquad (2.15) \qquad\qquad r = \sqrt{\frac{I}{A}} \qquad (2.16)$$

The capacity of a column, is highly dependent on slenderness and decreases as the slenderness increases, illustrated in Fig2.5. The stresses in the column are defined in Eq. 2.17.

$$\sigma_E = \frac{N_E}{A} = \frac{\pi^2 EI}{L^2 A} = \frac{\pi^2 E}{\lambda^2} \qquad (2.17)$$

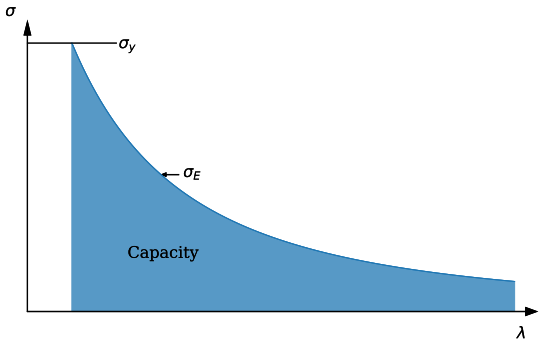

Figure 2.5: Eulers critical load dependency on slenderness.

Approximate solution

The Euler theory is, as mentioned, based on a linearized approach due to simplifications of the curvature of a deflected column as in Eq. 2.10. The exact curvature of a deflected column exposed to axial loading is given in Eq. 2.18 by Gere and Barry [26].

$$\frac{1}{R} = \frac{w_{xx}}{(1 + w_x^2)^{3/2}} \tag{2.18}$$

Guddal [4] presented an approximate solution for a critical load by conduct a series expansion based on the exact curvature. The approximate solution based on the exact curvature can then be obtained as in Eq. 2.19. The Euler load appears as conservative compared to the approximate solution, illustrated in Fig. 2.6. However, for small deflections, these two solutions are more than less the same. Euler's critical solution will, therefore, be utilized in this thesis.

$$\frac{N}{N_E} = 1 + \frac{\pi^2 \delta}{8 L_b^2} \tag{2.19}$$

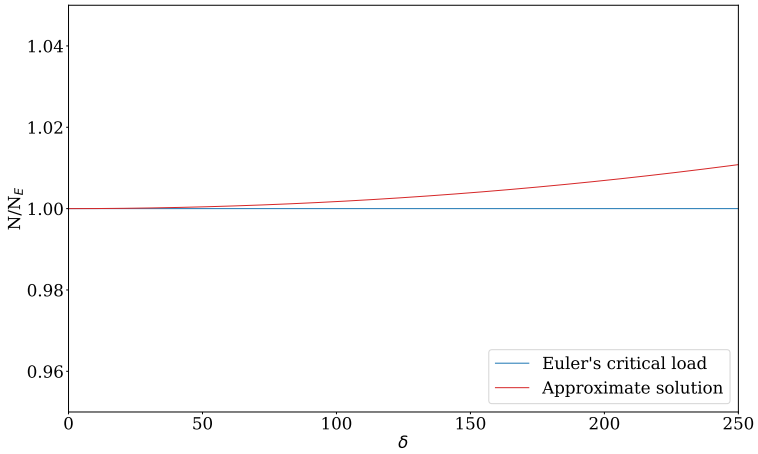

Figure 2.6: Euler's critical load compared with approximate solution based on exact curvature. $Lb = 2670mm, E = 70000MPa, I = 1222566.7mm^4$

Cross sectional capacity

Slenderness decides if it is dealt with a cross-sectional capacity problem, a geometrical instability problem, or a combination of them both. By implementing an initial deflection, the column is forced into a momentum state as Eq. 2.9 presents. As the column proceeds to deflect the momentum becomes severe. An interaction equation is, therefore, necessary to implement this contribution. The capacity is then defined by an expression that includes both momentum and axial loading, shown in Eq. 2.20.

$$\frac{N}{N_d} + \frac{M}{M_d} \leq 1 \tag{2.20}$$

Where: $N_d = \sigma_y A$ $M_d = \sigma_y W_y$ $M = N\delta$.

The interaction equation is limited by the yield stress of the material and implements the cross-sectional properties to limit the columns capacity.

$$N(\frac{1}{A} + \frac{\delta}{W_y}) \leq \sigma_y \tag{2.21}$$

For short columns with high cross-sectional slenderness the axial contribution in Eq. 2.21 will be the driving term. For long columns with high slenderness, the momentum contribution will be governing.

Initial deflection

Exposing an initially deflected column to further axial compression will trig a global buckling mode at an early stage of the process. A momentum will occur from the start of the loading due to the initial deflection illustrated in Fig. 2.7a. The momentum Eq. 2.9 will then be defined by a summation of the initial deflection ω_0 and further deflection ω produced by axial compression. By combining differential Eq. 2.13 with the new expression for deflection, the differential equation in Eq. 2.22 can be obtained. The solution of this differential Eq. are solved in App. B and results in the following Eq. 2.23 for the maximum deflection. N_{Cr} is a general term for critical load based on a simple sinus curvature. The initial deflection stabilizes the buckling propagation since it trigs the global buckling mode. A reduction of the slope in the load-displacement diagram occurs, illustrated in Fig. 2.7b. This makes it easier to retrieve the experience with high precision.

$$\frac{\pi^2 EI}{L^2} + r^2\omega = -r^2\omega_0 \qquad (2.22)$$

$$\delta = \delta_0 \frac{1}{1 - N/N_{Cr}} \qquad (2.23)$$

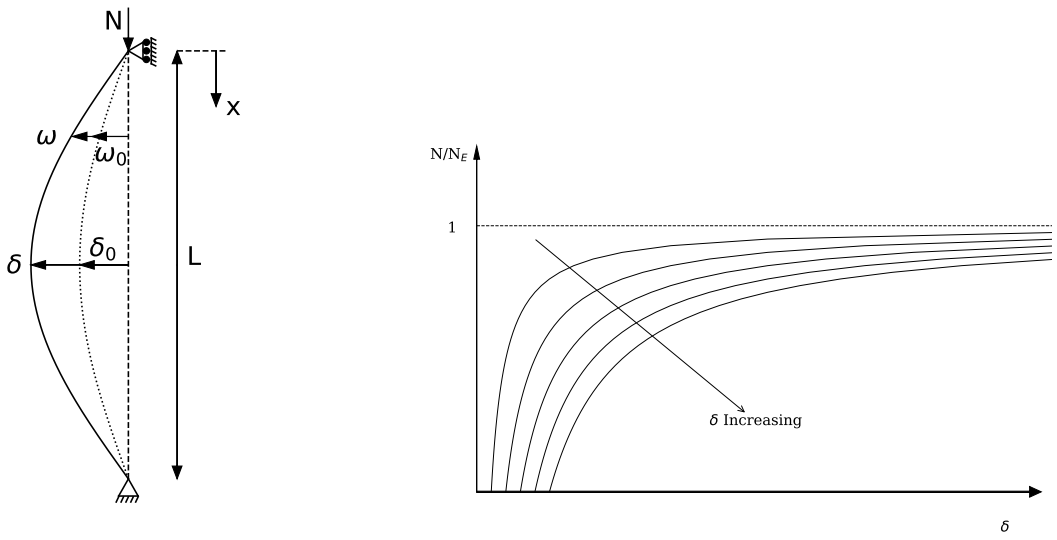

(a) Initial deflection. **(b)** Effect of initial deflection.

Figure 2.7: Effect of initial deflection.

Theoretical capacity

Euler's solution contains a theoretical proposal that is based on a global elastic buckling mode. A column exposed to axial compression with high column slen-

derness and low cross-sectional slenderness will typically conceive a global elastic buckling mode. Through the material properties, a yielding of the cross-section is sat as a limitation. To illustrate this the Euler's solution with initial deflection are plotted against the cross-sectional capacity in Fig.2.8. The intersection between the two solutions will be referred to as the elastic capacity load $N_{El.Cap}$. It should be emphasized that the predicted path is expected to bend off from the Euler's solution against the cross-sectional capacity, before reaching the buckling load presented by black dotted lines in Fig.2.8. The shaded are beneath the lines represents the elastic capacity of the column.

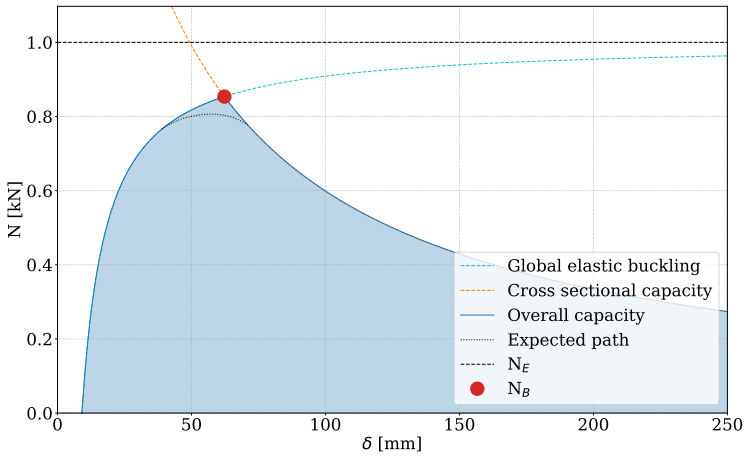

Figure 2.8: Intersection between cross sectional capacity and Euler capacity with initial deflection.

The theoretical approach has the power to overestimate the capacity of a column. A reasons for this is that local buckling is not implement as a restriction. Local buckling is, however, implemented in EC9.

2.5.2 Eurocode 9: Design of aluminium structures

The Eurocodes are a collection of advanced structural standards developed by an EU-collaboration or more specific the European Committee for Standardization in the order to ensure continuity and reliable constructions within the European Union. These standards are used in the design of load-bearing structures but are only a supplement and must always be used together with the national annex within each specific country [27].

As mentioned in the introduction the EC9 were used to establish a prototype of the power pylons which lowered the weight of the construction with nearly 40 % compared to the power pylons made of steel. Statnett wishes to decrease the weight in the range of 60-70 %. By exact experimental approach and simulations, it is possible to maintain a foundation to deviate from the standards and hopefully

reach these requirements. EC9 [5] are in these thesis utilized to make an analytic calculation. The calculations include both establishments of the critical load and the buckling load of members in bending exposed to axial load.

Classifications

The first step to define an analytic calculation based on the EC9 is to classify the problem at hand. The classes are divided into two groups where the first classification places the problem as either class A or class B, dependent on the material properties. This class is referred to as the buckling class and consists in tables, stated for different alloys and heat treatments. The second class is more complex to define, and are based on the slenderness in addition to stress gradient through the cross-section. This classification establishes the cross-sectional properties of the problem. The classification is in the range 1 to 4 where class 1 is a profile that is likely to achieve an elastic global buckling mode. Class 4 problems are expected to be limited by their cross-sectional slenderness, meaning that they are likely to achieve local buckling prior global buckling. Buckling is associated with compressional stresses. The area of interest is therefore the compressional side of the cross-section.

Analytic calculation

EC9 states that a compression member must be designed such that designed value for compression force N_{Ed} always must be less than or equal to the designed buckling resistance $N_{b,Rd}$. as in Eq. 2.24 where the buckling resistance load is defined in Eq. 2.25. The χ factor implements the elastic buckling capacity based on E, I and L_B to the buckling resistance formula. In addition to an imperfection factor and a limit of the horizontal plateau based on the material class.

$$\frac{N_{Ed}}{N_{b,Rd}} \geqslant 1 \qquad (2.24) \qquad N_{b,Rd} = \kappa\chi A_{eff}\sigma_0/\gamma_{M1} \qquad (2.25)$$

- κ is a factor that includes weakening effects due to welding
- χ is the reduction factor for the relevant buckling mode
- A_{eff} is the effective area
- σ_0 is the yield strength of the material
- γ_{M1} is the partial safety factor defined by national annex

A formula for members in bending and axial compression is given in 2.26.

$$(\frac{N_{Ed}}{\omega_{0,EC9}N_{b,Rd}})^{0.8} + \frac{1}{\omega_{0,EC9}}(\frac{M_{y,Ed}}{M_{y,Rd}})^{1.7})]^{0.6} \geqslant 1.0 \qquad (2.26)$$

- $\omega_{0,EC9}$ is a factor that includes weakening effects due to welding and holes
- $M_{y,Rd}$ is the bending moment about the y-axis
- $M_{y,Rd}$ is the bending moment capacity about the y-axis

2.6 Accuracy and precision

In science there are two important phenomena when it comes to evaluating experimental results, these are accuracy and precision and are described by G. Rodrigues [28]. These expressions are important to validate scientific research. Accuracy describes the degree of repetition done for every experiment while precision addresses systematically errors during the experiments. If the measurement retrieve the same results every time, the precision is high. If the experiment measure what it is supposed to, the accuracy is high. Illustrative figures of the phenomena are displayed in Fig. 2.9.

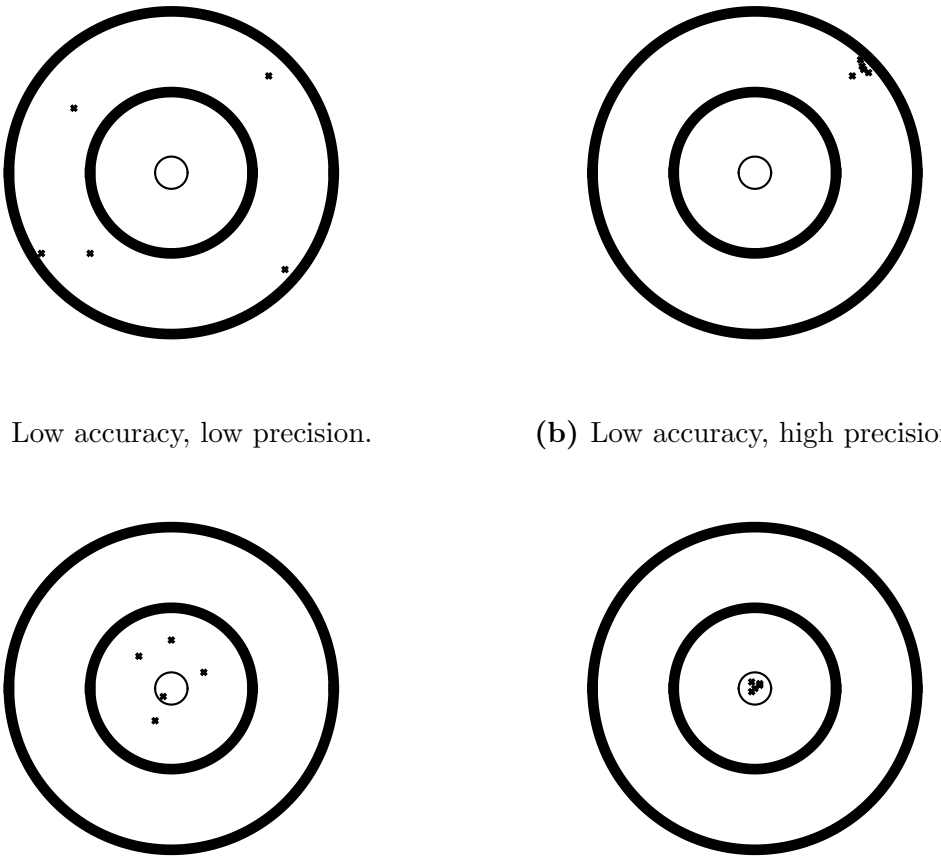

(a) Low accuracy, low precision.

(b) Low accuracy, high precision.

(c) High accuracy, low precision.

(d) High accuracy, high precision.

Figure 2.9: Accuracy and precision.

Chapter 3

Material calibration

To detect eventual material property differences, and to establishment a constitutive stress-strain relation, tensile tests has been conducted. The cross-section holds a hollow thin-walled rectangular, with a flange perpendicular to one of its major sides. Twelve dog bone specimen, or more specific UT80 specimens, were cut out from the columns cross-sectional area. The aluminium alloy in this study is a 6082-T6. The yield stress are therefore expected to occure in the range of 240 - 295 MPa [29].

This chapter presents the experimental process of the tensile tests, in addition to analysis performed through Digital Image Correlation (DIC). The establishment of the constitutive stress-strain relation is covered and a numerical analysis was conducted to validate the result.

Different material properties were to be found in the material. The flange of the cross section did achieve the least strict hardening law.

3.1 Tensile test

The tensile test was performed in an Instron 5982 testing machine at the laboratories of the department of structural engineering at NTNU. They are presented in Fig. 3.1a and fig. 3.1b respectively. The loading of the specimens was displacement controlled with a rate of 1 mm/sec. The amount of force applied to the specimens was traced by an internal load cell in the Instron test machine. The elongation was analyzed through use of a virtual extensometer utilizing DIC. The specimens were painted with a speckle pattern in order to trace the elongation of the tensile tests.

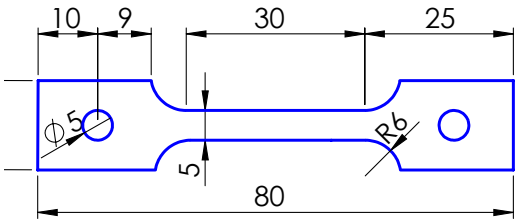

(a) Dog bone specimen - UT80

(b) Instron 5982 [30].

Figure 3.1: Tensile test specimen and instrument.

Three tensile test specimens were cut out in the longitudinal direction from the extruded aluminium profile at three locations illustrated in Fig. 3.2b. In addition, were three specimens were cut out in the transverse direction at the major side of the profile, denoted A in Fig. 3.2b. The specimens are named by two letters and a number. The first letter indicates which of the sides the specimen is withdrawn, as shown in Fig. 3.2b. The second letter indicates if the specimen is cut out in either the longitudinal, L, or the transverse, T, direction. The number of the two digits states which one of the three specimens it is referred to. AL-1 is then the first specimen withdrawn from the major side, and in the longitudinal direction. Measurements were completed in both height and thickness at three different locations illustrated in Fig. 3.2a. The measurements reveal that there is an undesirable ratio between the width and height of the dog bone specimens. Normally, a specimen has a high height-thickness ratio in an attempt to avoid microstructure defects within the tensile tests. The chances of containing material defects increase with the transverse area of the specimen [18]. This could result in an undesired variation from the stress-strain curves extracted from the same test series.

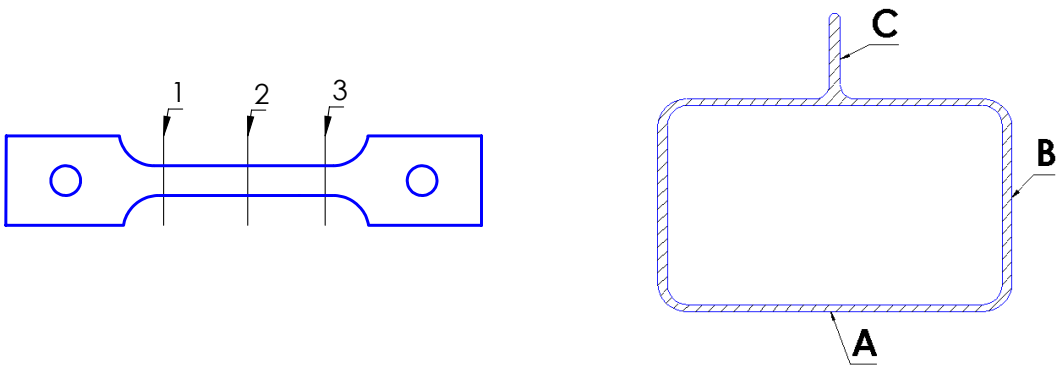

(a) The measurement locations in Tab. D.1 are illustrated.

(b) Profile sides specification are illustrated.

Figure 3.2: Definition of the measurement labeling

The mode of every measurement of both height and width of the tensile test are displayed for every series in Tab. 3.1.

Table 3.1: Tensile test mode of the measurements

Test series	$h \times w$
AL	4.99×2.32
AT	4.99×2.31
BL	4.99×3.48
CL	4.98×4.01

3.2 Digital image correlation - DIC

There are several different ways to read the deformation pattern from a tensile test. DIC is an optical technique which is able to measure contour, deformation, vibration and strain on almost any material [31]. Multiple frames were logged throughout the tensile tests and then analyzed with eCorr which are the DIC software used in this study [13]. The AL-1 specimen are used to illustrate the analysis procedure in the Fig. 3.3. The specimen is painted with a speckle pattern, Fig. 3.3a, that is used to track the displacement field of the specimen. A mesh is added above the speckle pattern, Fig. 3.3b, and within the gauge area where the plastic strains are assumed to occur. The mesh is locking the speckle pattern within each element and traces the contour in an attempt to remain a grayscale equilibrium within the boundaries[32].

Using eCorr a mesh was attached on top of the stress-free specimen at frame 1. The mesh consists of Q-4 elements of size 25*25 pixels illustrated in Fig. 3.3b. As the specimen is exposed to tension, the mesh will stretch out in an attempt to keep the grey scale of the specimen within its boundaries. The Q-4 elements do only obtain translation degree of freedom to the corner nodes. The path between

the nodes will remain of the first order. The elements will, therefore, force a linear strain distribution [33].

DIC could be used to analyze strains in the necking area by observing both the longitudinal and transverse direction. This to subtract data after necking has occurred. Due to the low strains that are expected to occur in the buckling analyses, this was omitted in these studies. Instead, the elongation of the specimen is extracted by a vector added through the gauge area as illustrated in Fig. 3.3c.

The necking is assumed to occur within the gauge area which is clear from Eq. 2.2 that states that the stresses are pathological dependent on the cross-section area. The necking is illustrated in Fig. 3.3d.

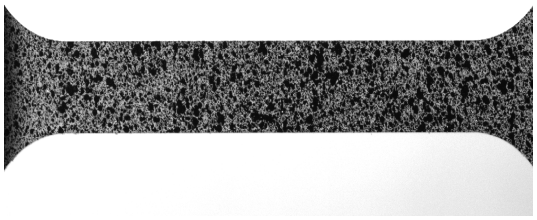

(a) Stress free with speckle pattern applied

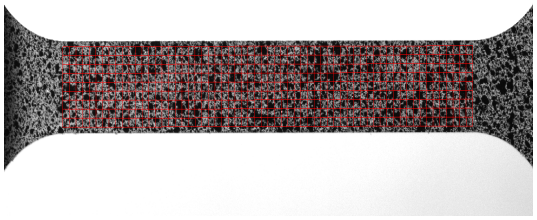

(b) Stress free with Q4 mesh applied

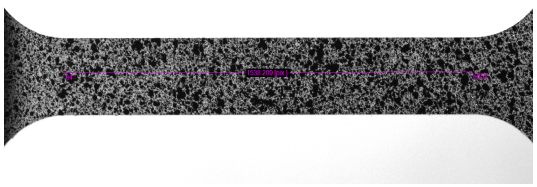

(c) Vector that was used to measure elongation

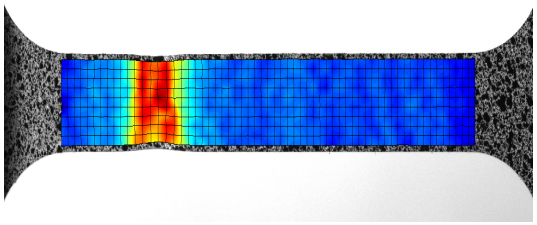

(d) Maximum strain before failure with stain field map applied

Figure 3.3: Illustrations from DIC analysis

A load cell integrated into the Instron 5982 test machine displayed in 3.1b, will log the applied load at multiple frames. There are roughly 800 frames logged for every specimen. By performing the DIC analysis the elongation, or the engineering strain, are withdrawn to the corresponding frame. By plotting the force-engineering strain curves the precision within each series appears to be high, illustrated in Fig. 3.4.

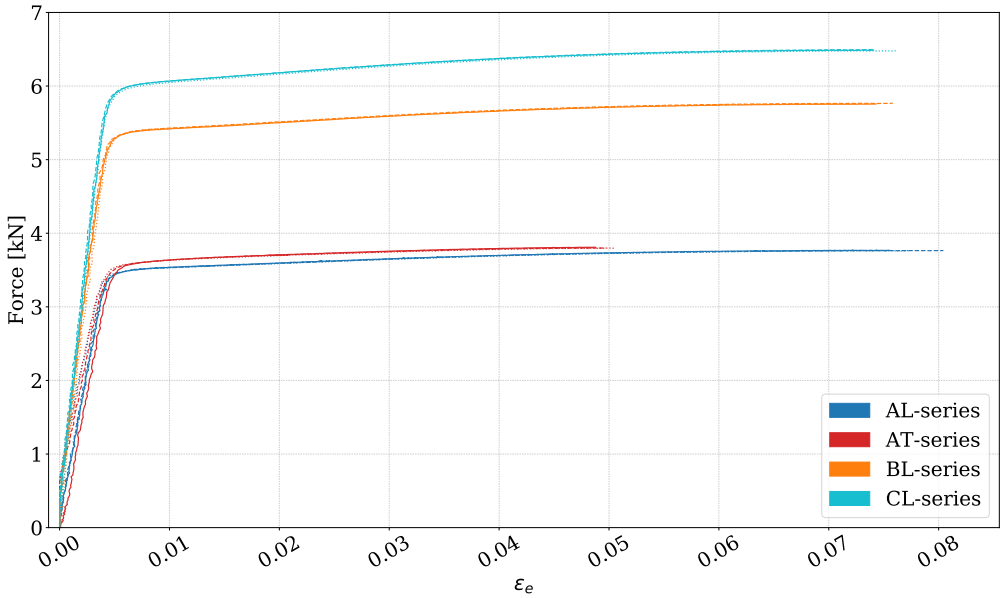

Figure 3.4: Raw data from DIC analysis. Engineering strain-force.

3.3 Post processing DIC

To obtain a constitutive stress-strain relation that can be implemented into Abaqus, the raw date needs to be post-processed. The first step is to obtain the true stress-strains by implementing the data into Eq. 2.2, 2.3 and 2.5. The engineering stress-strains are based on a constant cross-sectional area off the specimen. The true stress-strain is based on a reduction of the cross-sectional area when exposed to tension. When converting, an elevation of the stress-strain curve will occur since the stresses will rise when the force is concentrated in a smaller area as the cross-sectional area, reduces illustrated in Fig. 3.5. Since the elongation is subtracted in the longitudinal direction of the dog bone specimen, it is not possible to contradict how the material behaves after necking. The strains was therefore deleted post the ultimate tensile stress.

A weakness by apply 2D-DIC analysis to a tensile test is the uncertainty of how the specimen do behave into and outwards of the plane. For example, if the specimen is bent outwards of the plane i.e. close up to the photo lens, the initial movement of the specimen will be to straighten this geometrical defect. The image will then

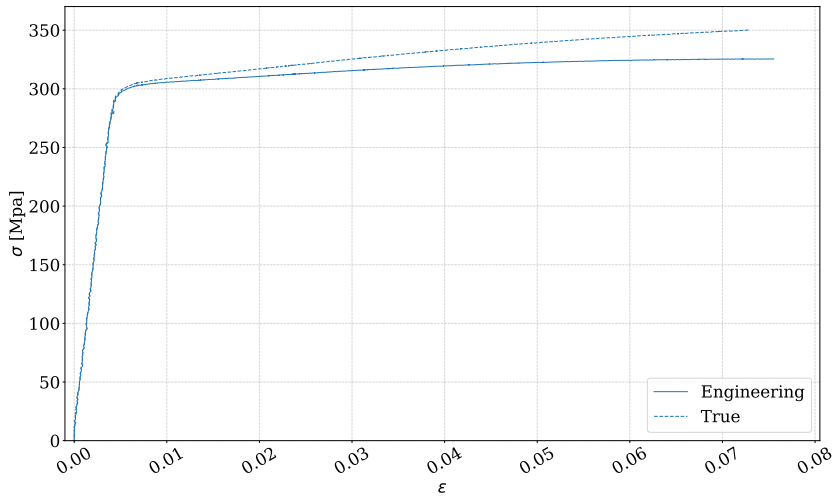

Figure 3.5: Engineering vs. true stress-strain.

result in a speckle pattern that reduces. DIC will analyze this as a compression of the specimen. The first strains are then to be negative. When the initial defect is stretched out and the specimen starts to actually stretch, the strains will rise as positive. This is illustrated by tensile test AT-2 in Fig. 3.6. All the negative strains was sat to zero. An implication of this phenomena is that the curve is translated towards a negative initial strain. To compensate, linear regression was conducted through a representative amount of data points in the elastic range and translated such that the initial strain starts at zero illustrated in Fig. 3.6.

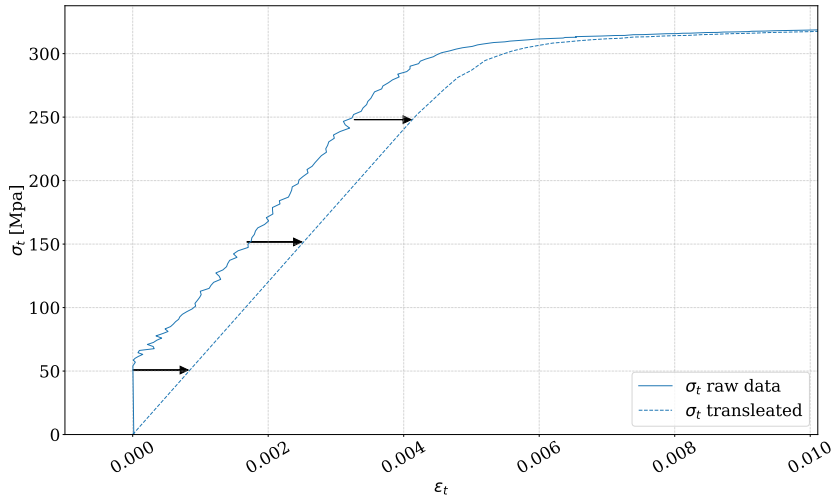

Figure 3.6: Transelate the ϵ_0 to origo.

Numerical noise is disturbances caused by the virtual extensometer applied in eCorr. This disturbance can be caused by vibrations and shifting in light during testing, in addition to the Q4-element characteristics. Linear paths and only translation degree of freedom in the nodes makes a strict deformation pattern of the elements and uneven strain distributions will be difficult to capture. A linear regression were conducted in the order to smooth data i.e. damp numerical noise.

Also, to compose an evenly distributed true strain vector such that every point in the data set could be averaged within the tensile series 3.7.

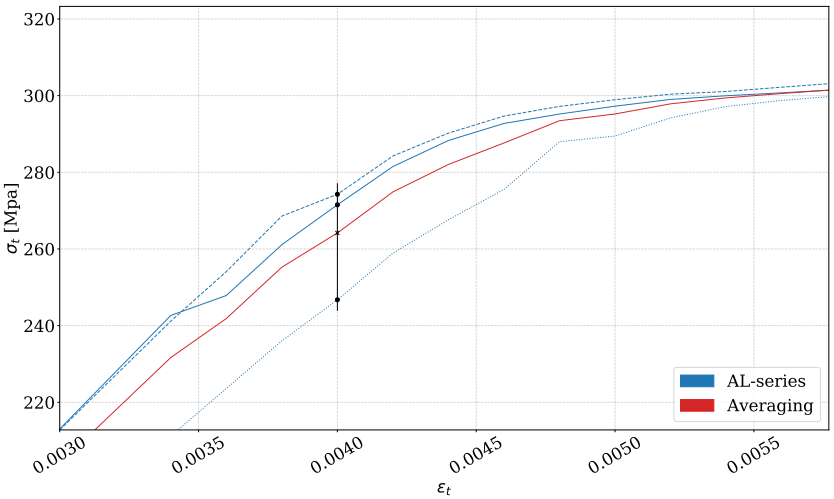

Figure 3.7: Smoothing the true stress-strain data points.

Due to the numerical noise, it does occur some uncertainty to the elastic region of the tensile test. A common procedure to handle this uncertainty is, therefore, to define the elastic region by a Young's modulus of 70 000 MPa, practiced in this study.

Yielding in the material can be difficult to determine due to a smooth transition between elastic and plastic strains. It is common to utilize a 0.2% offset method. In this study it was found that a 0.2 % offset method did erase a significantly amount of data, displayed in Fig. 3.8. The yield point was therefore defined by a 0.02 % offset method to represent the plastic regime in a more accurate manner.

To define a hardening rule that defines hardening evolution of the plastic strains in the material. This were done by optimizing a function to obtain a constitutive stress-strain relation of the plastic region. A common hardening law of that usually corresponds well the the aluminum hardening evolution is the voice hardening rule. Voce law is a summation rule presented in Eq. 2.7. Two summations were used in this study. The different Voce rules optimized against the different series are shown in Fig. 3.9.

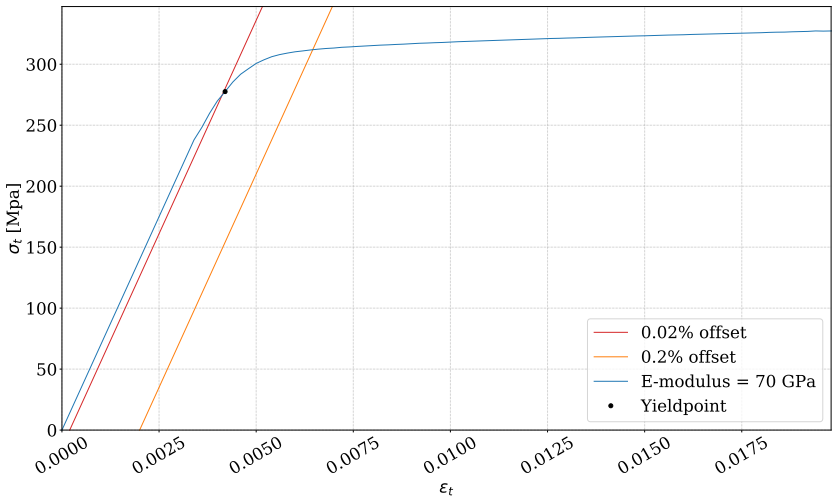

Figure 3.8: Defining the yieldpoint by 0.02% offset method.

3.3.1 Constitutive stress-strain relation

It does consist uncertainties while analyzing the elastic region of a tensile test with 2D-DIC due to numerical noise. The final constitutive stress-strain relation for all series consists of a elastic region where Hooke's law is applied as a liner relation through the Young's modulus of 70 000 Mpa given in Eq. 2.4. For the plastic region the constitutive relation is based on a Voce hardening rule of 2 summations which does vary between the series illustrated in Fig. 3.9.

The precision within the tensile series remained high, but does vary between the series. Participation hardening does reduce dislocations in the lattice of the material and increase the yield strength described in Sec. 2.2 in Ch. 2. It is reasonable to believe that there is some correlation between wall thickness and hardening of the material. A thick wall is expected to achieve a longer cooling period than a thin-walled region. There is, however, no clear connection that states this hypothesis by observing the curves in Fig. 3.9. However since the flange do have a free surface at both sides, this region seems to achieve a cooling process more efficient than the two other regions. The remaining regions, A and B, does include one of its surfaces to face the inside of the column. The cooling process is then to be assumed less efficient, since the convection is lower [34]. It is reason to believe that the flange do obtain the softest hardening evolution since it does achieve a the shortest participation hardening process. These data is further implemented into the numerical model of the column to achieve a conservative rather than a non-conservative result. The Voce hardening parameters are displayed in Tab. 3.2.

One important implication of the choice of when defining material properties, is that low plastic strains are expected to occur in the experimental bending in this study. I.e. is the energy absorption expected to mainly appear as elastic strains. This needs to be validated and is going to be discussed in Ch. 7.

Table 3.2: Voce hardening rule parameters.

Description	σ_0 [MPa]	Q_1 [-]	C_1 [-]	Q_2 [-]	C_2 [-]
AL	282.1	81.0	13.4	20.4	1808.9
AT	277.6	59.8	19.6	34.1	1375.3
BL	295.2	80.0	13.5	13.8	2072.1
CL	282.2	78.2	15.0	16.8	1849.0

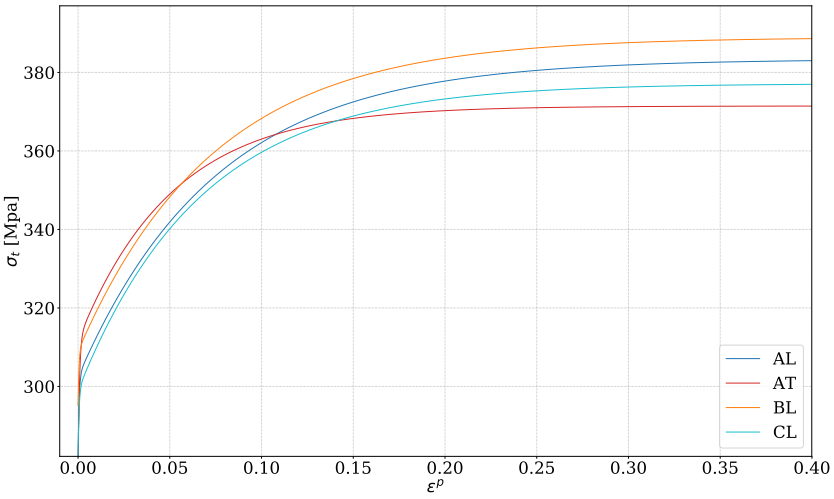

Figure 3.9: Voce rule optimized to obtain a constitutive stress-strain relation for the plastic region of the material.

3.4 Numerical implementation

To secure that the numerical model in Abaqus do achieve the material response desired, the tensile test were recreated in Abaqus. The density, elastic properties and plastic properties defined by Voce hardening rule were denoted to the four different tensile tests. It is expected a tight correlation between the numeric analysis and the experimental data. The true stress-strain curves for the experimental data, the data implemented into the numerical model and the numerical results are compared in Fig. 3.10 for the AL-series. The curves are more than less a copy of one another which it should be if the calibration is done right. This indicates that the constitutive stress-strain relation is valid and calibrated in a sufficient manner such that it can be used in the development of the numeric model. The corresponding plots for the remaining tensile test series are plotted in App. C.

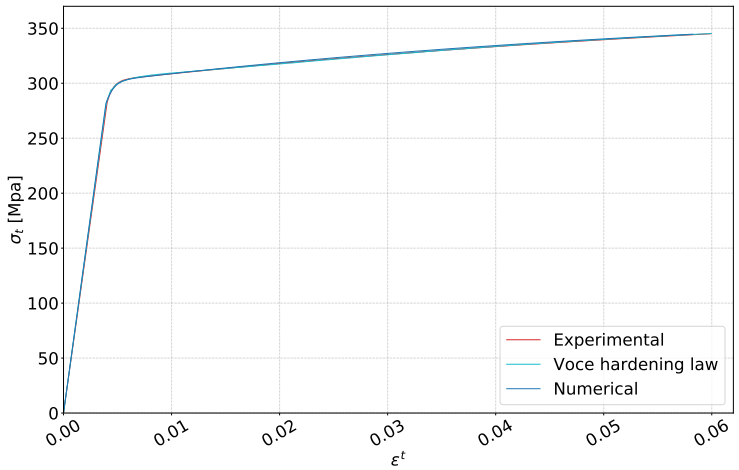

Figure 3.10: The tensile test compared between numeric and experimental results for the AL-series.

Chapter 4

Laboratory setup

The experimental setup belongs to CASA and is located at the Department of Structural Engineering at NTNU. It has been improved through the last 3 years by Ph.D. Marius E. Andresen and Professor Magnus Langseth in collaboration with Sigurd Guddal, Andreas V. Nesje, Pål A. Nilsen, Niklas Amundsen and Aksel Lynum. Despite the simplicity of the experiment, the recreation in a laboratory has its challenges. First of all the dimension of the columns, that can be as tall as 4.5 meters, poses certain demands to the supporting construction. Obtaining frictionless bearings that sufficiently reproduce freely supported boundary conditions has also been a challenge. A transverse loading of the column has been applied where it has been difficulties to establish this loading in a static manner. Further, has it been essential to capture precise measurement data.

4.1 Components and dimensions

The experimental setup was located at the department of structural engineering at NTNU. The setup was custom made to reproduce a large scale global buckling with rotational free boundary conditions of columns up to 4.5 m. The purpose is to better understand the capacity of aluminium columns exposed to both bending and axial compression.

The experimental setup consists in its general form of a column exposed to a static transverse mid-span load and axial compression. The supports at the boundaries are simply supported, i.e. free to rotate. The column is mounted into the supports at a distance L_1 from the rotational center illustrated in Fig. 4.1. The length measurements of the column in this specific thesis are listed in Tab. 4.1. It is possible to either lower or elevate the upper supports to examine different column lengths.

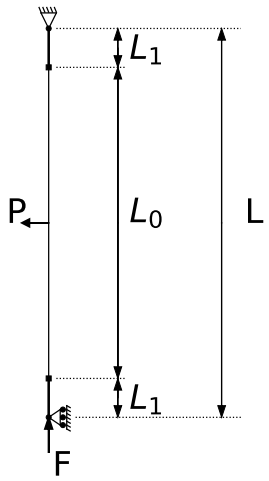

Figure 4.1: The experimental setup

Table 4.1: Column specification

Distance to rotational center	L_1	85	mm
Initial column length	L_0	2500	mm
Total column length	L	2670	mm

4.2 Transverse loading

A transverse load that remains static throughout the complete buckling process is applied through a pulley system. A wire holds constant weights, Fig 4.2a, coupled through the pulley system, and attached to the column by a strap, Fig. 4.2b. The strap has a width of 2.5 cm and was connected to the wire through a load cell. This to measured the force applied to the column to account for fictional loses in the pulley system.

As mentioned in the introduction of this chapter, the column was exposed to buckling in both directions about the weak axis. This implies that the flange in the profile was exposed to either tensional or compressional stresses. To trig the column in one of the two different bending modes the horizontal load was attached differently. Either to pull the column into a state that exposes the flange to tension, Fig. 4.2c, or to compression, Fig. 4.2d. In the purpose to distribute the pressure from the strap applied to the column, wooden bricks where attached as spacers about the flange.

(a) Weights coupled to wire.

(b) Wire connected to column through pulley system.

(c) Connection between pulley system, load cell and column for the FC-series.

(d) Connection between pulley system, load cell and column for the FT-series.

Figure 4.2: Laboratory setup for the transverse mid span loading.

4.3 Supports

The supports should apply small frictional forces to the system, for the column to be considered as simply supported. Two massive supports are therefore implemented in the setup and illustrated in Fig. 4.3a and 4.3b. The bottom support is free to rotate and possess the freedom to translate in the axial direction of the column. A hydraulic pressure piston that applies the axial compression force to the column is mounted beneath this support. The upper support is on the other hand fixed in translation, jet free to rotate.

The column is further attached to the supports in custom-made mounts by placing it into milled tracks that fit the profile. The milled tracks are 10 mm deep and the bottom of the mounts are at a distance of 85 mm from the support of the rotational center. This results to a total buckling length of $2500mm + 2 \times 85mm = 2670mm$. The supports are aligned by attaching a screw into a pre-made screw hole at the mass center of the upper mount and further attached to a thread with a pointy solder. The gravity secure leveling of the solder is made such that the bottom support can be calibrated against the top support, to secure vertically alignment. The calibration process of the alignment is illustrated in Fig. 4.3c.

(a) Bottom support. **(b)** Top support. **(c)** Alignment procedure of the supports.

Figure 4.3: Laboratory setup for the supports.

4.4 Measurement

There are in total 5 sensors attached to the experimental setup. Two sensors to measure the vertical and horizontal loading. Two lasers to measure the vertical displacement of the upper and the bottom support, to validate that only the bottom support moves during the process. These two sensors also measure the angle of the upper and the bottom support to observe the rotations of the supports. A sensor measures the displacement of the column at a distance of 1473 mm above

the lower rotational center. By assuming a sinus-shaped deflection pattern along the buckling length of the column, the mid-span deflection can be obtained. The total content in the laboratory setup is presented in Tab. 4.2.

Table 4.2: The experimental setup content.

Description	Quantity	Explanation
Sensors	2	For measure the vertical displacement and rotation both in the lower and in the upper support.
	1	To measure the transverse load at the midpoint of the column.
	1	To measure the transverse displacement of the column.
	1	To measure the axial compression.
Rotational joints	1	In the lower support free to rotate about the weak axis of the column.
	1	In the upper support free to rotate about the weak axis of the column.
Carrying constructions	1	To mount the column within.
Standing construction	1	Attach sensors separated from the carrying construction to avoid disturbance.
Hydraulic pressure piston	1	To apply axial load.
Custom made mounts	2	To attach the column in the lower and upper supports.
Weights		Used for horizontal mid span load.
Pulley system		Used to attach horizontal mid-span load.
Software		To log data.
Hardware		To log data.

Chapter 5

Laboratory experiments

The laboratory work consisted of eight different tests divided into two groups, further divided into two subgroups. Simply supported aluminium columns of length 2500 mm were exposed to axial compression about the weak axis. A static transverse mid-span load was applied. The column at hand holds an unsymmetrical cross-section assembled by a hollow, thin-walled rectangular, and a flange perpendicular to one of its major sides. The column was exposed to bending in both directions about its weak axis. The two main groups are referred to as the FT- and the FC-series. It denotes whether the flange is exposed to either tensional nor compressional stresses, respectively.

High cross-sectional slenderness implements local buckling as a possible failure mode. This chapter will present the experimental work and results, in addition to discussions the implications of the different tests.

The experimental testing was conducted at the Department of structural engineering at NTNU the 22 of March 2018. Illustrations that does include axial compression force against mid-span displacement are referred to as force-displacement.

5.1 Study presentation

The cross-section addressed in these studies is presented in Fig. 5.1. The cross-section is divided into three sections. That is the major side A, the minor sides B, and the flange C, as illustrated in Fig. 3.2 in Ch. 3. The flange breaks the symmetry, and as a consequence, translates the neutral y-axis. This provided a more complex problem. The slenderness of the column is significantly high, which also accounts for the cross-section. A clear weakness appears for the major side, which holds high slenderness of about 50, making it exposed to local buckling. The local slenderness of the cross-sectional parts is calculated in App. F.

The cross-section is symmetrical about the Z-axis. Profile specification is given in Tab. 5.1.

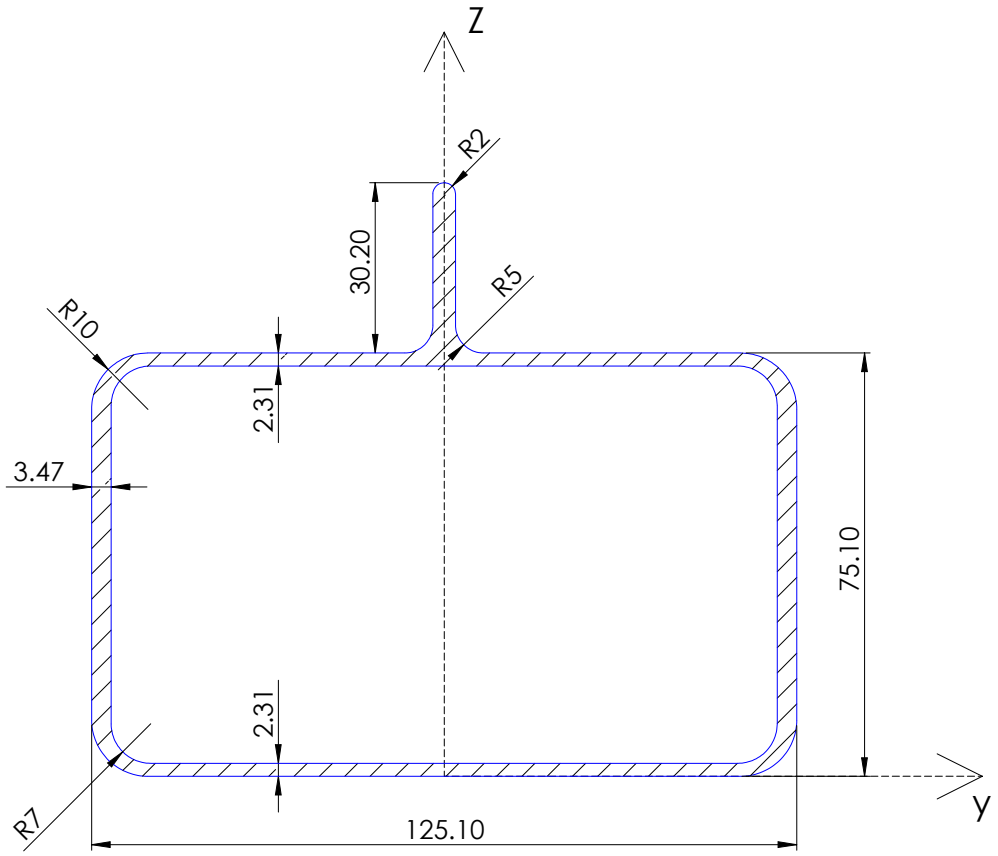

Figure 5.1: Profile dimensions. All measures in mm.

There were in total completed eight tests with four different test setups, divided into two main groups. Four tests were conducted by exposing the cross-sectional area such that the flange retrieved tensional stresses. These tests are referred to as FT-series. During the four remaining test, denoted as FC-series, the flange was exposed to compression. These test series were further divided into two groups. Two tests exposed the column of a transverse mid-span load of 200 kg, and two tests exposed the column for a transverse mid-span load of 100 kg. The test

order can be shown in Tab. E.1 in App. E. A test is denoted with both flange stress state, transverse load and a number that indicates which of the two tests it is referred to. FT-200-1 refers to test number 1 where flange was exposed to tensional stresses and a transverse mid-span load of 200 kg was applied.

Table 5.1: Profile specifications

Cross sectional area	A	1153.1	mm^2
Yield stress	σ_0	282.2	MPa
Neutral y-axis	C_y	43.3	mm
Neutral y-axis of rectangular section	C_{0y}	37.55	mm
2. area of momentum	I	1222566.7	mm^4
Elastic section modulus	W_y	19726.8	mm^3
Column slenderness	λ	82.0	[-]
Relative slenderness	$\overline{\lambda}$	1.7	[-]

5.2 Experimental results

The tests that encountered the least capacity was the FT-200 series with a buckling load of 83 kN. The FC-100 series achieved the highest buckling load in the range of 112 - 114 kN. The experimental data are plotted as axial loading against mid-span displacement, referred to as force-displacement, in Fig. 5.2. It is limited by maximum displacement where unloading of the column was initiated. It should be emphasized that the actual transverse mid-span loading decreased somewhat, compared to the applied load. This was caused by frictional losses in the pulley system, used to connect the weights to the column. The load decreased with roughly 10 %. The mean of the measured transverse mid-span load is presented in Tab. 5.2. The deflection of the column was measured at a distance slightly above the mid span of the column. The mid-span displacement was obtained by assuming that the column did deflect as a sinus curve.

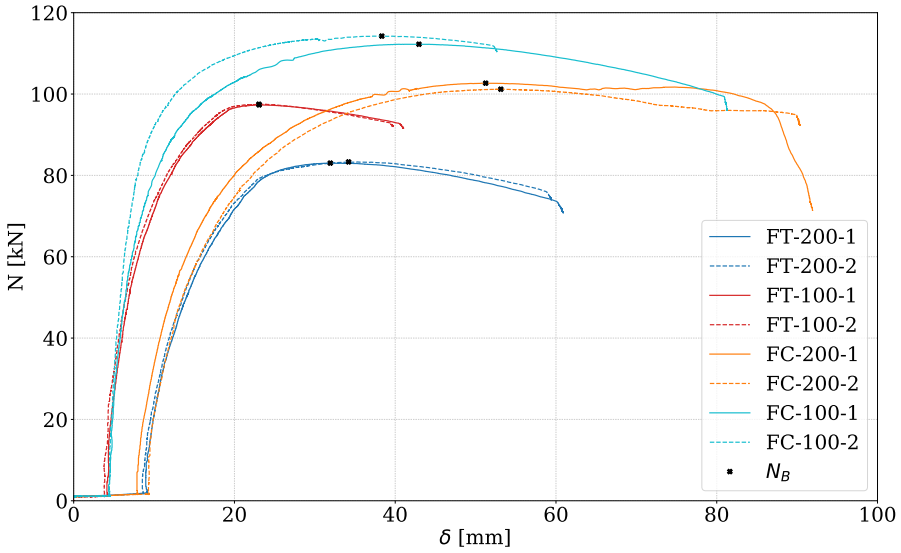

Figure 5.2: Experimental mid span displacement against axial load.

5.2.1 Comparison within the series

The deviations within each test are presented in Tab. 5.3, where the definitions of Δ_δ and Δ_N are illustrated in Fig. 5.3. Small deviations imply that the experiment precision of the experiment is high. By increasing the transverse load from 90 kg to 175 kg, the capacity of the column undergoes a significant reduction. For the FT-series this reduction is nearly 15 % while the FC-series decreases by 9 %.

The largest deviation for the initial displacements is observed for the FC-200 test-series, with approximatly 1.3 mm. This, regardless of the coincident between

Table 5.2: Experimental measurements.

Description	δ_0 [mm]	F [kg]	N_B [kN]	δ at N_B [kN]
FT-200-1	9.1	175.9	83.0	31.9
FT-200-2	8.7	174.8	83.3	34.2
FT-100-1	4.2	89.2	97.3	23.1
FT-100-2	3.8	88.7	97.5	23.0
FC-200-1	8.0	174.5	102.7	51.3
FC-200-2	9.3	174.8	101.2	53.1
FC-100-1	4.4	89.9	112.3	43.0
FC-100-2	4.5	89.1	114.3	38.3

the transverse loads. The slope of these curves is, despite this, fairly similar. The buckling loads reflect the divergence in initial displacement with a delayed peak. This indicates that the measurement of the displacement might have some irregularities, and that the columns response within this series is fairly similar.

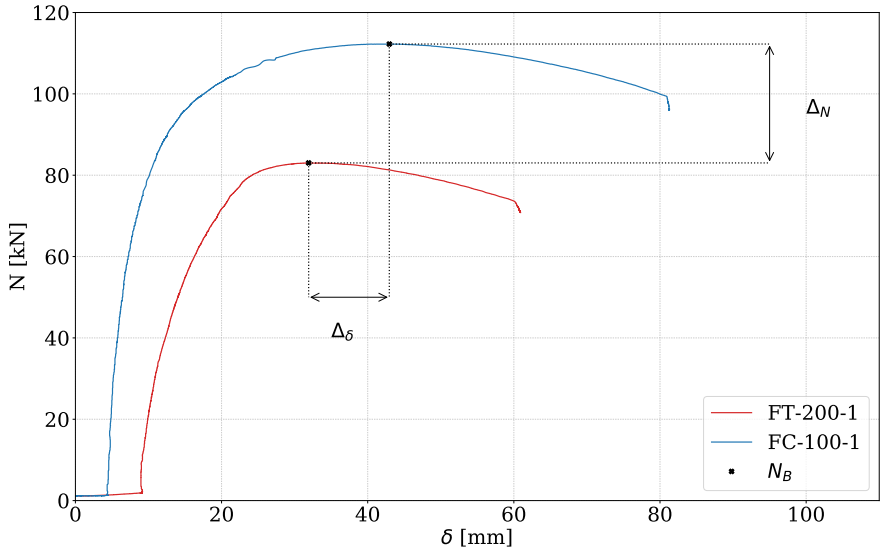

Figure 5.3: Definition of Δ_δ and Δ_N.

The FC-100 test-series stands out as the slopes separate when the columns approach their buckling loads. The midspan displacement deviation,Δ_N, obtains a difference of 11 %. Despite the initial displacements being more or less the same, presented in Tab. 5.2. The FC-100-2 test achieves high opposition to deflection.

Exposing columns to axial compression without initial deflection would lead to low precision. Buckling is an instability problem where a small increase in applied load is met by a large deflection. This is a result of external forces, first met by internal stresses in the column, force an instability, which triggers the internal force to evolve into bending moment. The tests were completed with an initial deflection to reduce the instability when approaching buckling.

Table 5.3: Comparison within the series. Absolute values.

Description	Δ_N [kN]	Δ_N [%]	Δ_δ [mm]	Δ_δ [%]
FT-200	0.29	0.3	2.28	6.7
FT-100	0.17	0.2	0.03	0.1
FT-200-1, FT-100-1	14.3	14.7	8.8	27.6
FC-200	1.48	1.4	1.88	3.5
FC-100	2.00	1.8	4.62	10.7
FC-200-1, FC-100-1	9.6	8.5	8.3	16.2

The FT-100 test-series shows the highest buckling loads. This implies that the instability, when approaching its capacity, will be sever compared to the other test series. Small disturbances will, therefore, have a considerable effect on the response of the columns. This can explain why the FT-100 series exhibit the lowest precision. Fig. 2.7b illustrates how high initial displacements enter a smooth transition towards maximum capacity, while a low initial displacement retrieves a sudden changeover.

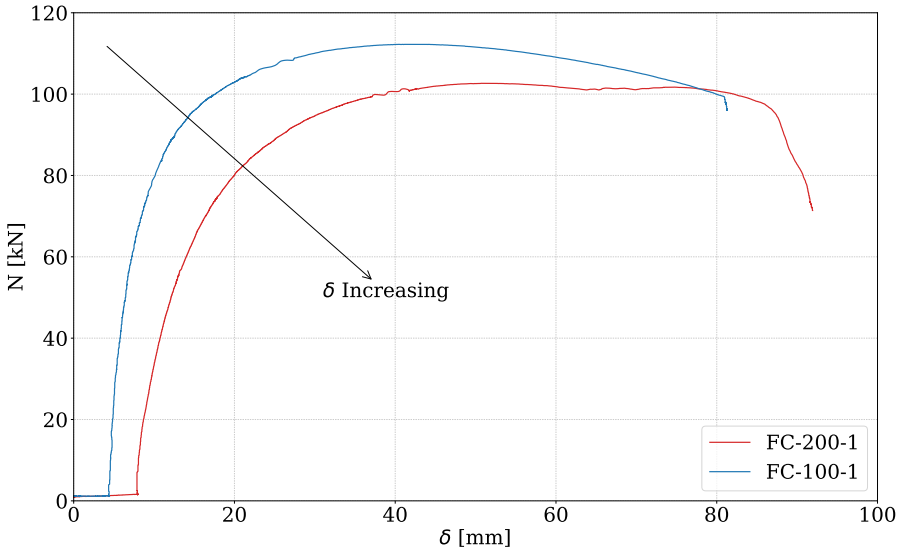

Figure 5.4: Implication of initial deflection illustrated by experimental results.

There is a clear correlation within the different test series. An overview of Fig.5.2 together with Tab. 5.2 indicates that the precision is high. In further comparison, the first test in each test-series will, therefore, be utilized if not stated otherwise. This both to simplify, and due to the high precision characterizing for the actual series.

5.2.2 Comparison between the series

There is a modest deviation between the initial displacement between the FT- and the FC-series. When the transverse load decreases by $\frac{1}{2}$, it seems to be met by a similar deflection response. This should be reasonable since there are low strains present in the column at these small displacements. As the strains remain elastic, it is expected more or less the same behavior between the series. This is substantiated by Euler's critical load where only the elastic properties, i.e. E and I, are applicable. However, as the axial load is increased, the FC-series exhibits a higher capacity than the FT-series. The FT-series had a significant drop after reaching its maximum capacity. The FT-series seemed to be more ductile and kept its strength even for high displacements. Some phenomena have to provoke this behavior.

Observations during the experimental testing on the FT-series revealed a local buckling pattern. The pattern occurred in short time prior buckling and are displayed in Fig. 5.6b. There are reasons to believe that the local buckling provoked a global buckling of the column, and by far limited its capacity.

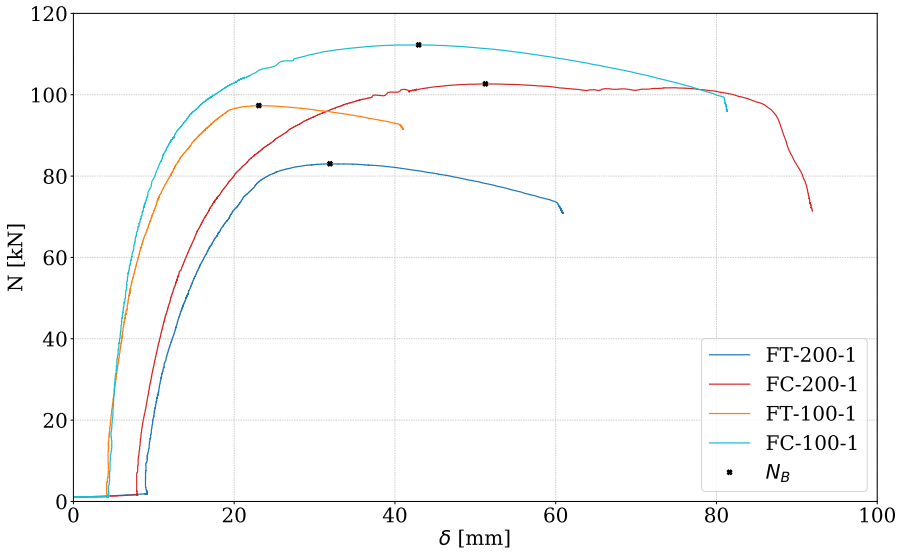

Figure 5.5: Comparison between the series.

The column shows the highest capacity for the FC-series for both transverse loads. Not only for the buckling load, but also for the deflection for where the buckling load is reached. The flange of these series first obtains a local buckling mode at significantly high deflections. The local buckling of the flange is pictured in Fig. 5.6a. It should be emphasized that this occurred beyond global buckling, for displacements above 70 mm.

(a) Local buckling of the flange exposed to compression.

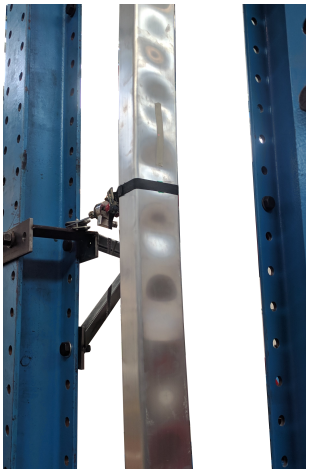

(b) Local buckling pattern that occurred in experimental testing for the FT-series.

Figure 5.6: Capacity of the FC-series.

The FC-200 tests produce an axial load capacity of nearly 20 % compared to the FT-series. In addition, they reach maximum axial load at a displacements 40 % higher. For the FC-100 and FT-100 tests, these numbers are respectively 15 % and 46 %, presented in Tab. 5.4. This states the effect of the flange and the effect of the columns bending direction.

Table 5.4: Comparison between the series. Absolute values.

Description	Δ_N [kN]	Δ_N [%]	Δ_δ [mm]	Δ_δ [%]
FC-FT: (200-1)	19.7	19.2	21.4	40.2
FC-FT: (100-1)	15	13.4	19.9	46.3

5.2.3 Interpretation

The column slenderness in the problem is 82, which is significantly high and makes it sensitive for transverse loading. By reducing the transverse load the with a factor off $\frac{1}{2}$ the buckling load N_B was increased with 15 % and 9 % for the FT-, and FC -series, respectively. This illustrates the large effect of implement bending to an axial compression problem.

The precision of the experimental data has been discussed. It is bad practice to conclude whether a precision is high or low based on two similar tests. However, as both test series within the FT-series did achieve remarkably high precision, it substantiates the hypothesis of high precision. The same account for the low precision within the FC-series.

The precision within the tests seems to increase with the transverse loading. This illustrates the importance of the transverse loading as it would have been difficult to achieve high precision for tests conducted only by axial compression. The

FT-series does achieve a remarkably high precision compared to the FC-series. This can be an implication of the local buckling pattern that does localize the instability problem. The FC-series, on the other hand, seems to undergo a pure elastic global buckling propagation. As the column approaches the bifurcation point, i.e. instability, it will enter the secondary path of the buckling process, as presented in Ch. 2. The secondary path is described as the point where a small increase in axial load is met by a large deflection respond. If the column achieves the secondary path on a global rather than a local level, it is reasonable to expect that this influences the deflection of the column to a greater extent.

Chapter 6

Analytical approach

In this thesis, two analytical approaches were examined and compared to the experimental results. A theoretical approach, limited by the restriction of elastic material behavior. Based on Euler's critical load with initial deflection, and yielding of the cross-section. The other approach is determined by the constructional standard "Eurocode 9: Design of Aluminium Structures, Part 1-1" referred to as EC9 [5].

6.1 Introduction to the analytical approaches

The theory used to obtain the analytic calculations is given in Ch. 2. The theoretical approach includes Euler's critical solution based on elastic bending of the column with initial deflection, where deflections follow a simple sinus curvature. As the deflections become significantly high during the bending process, the cross-section is expected to yield. A two-step limitation for the bending propagation is therefore implemented into the theory. One to be described by an elastic bending propagation. The other to implement yielding of the cross-section referred to as cross-sectional capacity.

Euler' critical solution is a linearized approach. It is expected to underestimate the capacity of the column. However, this underestimation should be negligible as discussed by comparison to the approximate solution in Sec. 2.4 in Ch. 2. It is, therefore, predicted that the theoretical bending propagation sufficiently describes the experimental data.

The cross-sectional capacity implements yielding in the material as a restriction. The aluminium will exhibit strain hardening, increasing the yield stress. It is, therefore, a possibility that the experimental data exceed the theoretical cross-section capacity.

To compare the experimental values to the capacity suggested by the theoretical solution, the elastic capacity load ($N_{El.Cap}$) is defined as in Fig. 6.1. It should be emphasized that this load is defined as the intersection between elastic bending capacity and cross-sectional capacity. The expected path of the column is, however, estimated to bend off, while approaching this intersection. The transition will be smooth and not abrupt as the actual intersection between these curves.

As the theoretical approach represents a straightforward calculation, the EC9 contributes to a more comprehensive approach. To calculate a critical load of an aluminium column a buckling class needs to be defined by the alloy at hand. The 6082-T6 is classified under buckling class A. In addition, a cross-sectional class needs to be established. In this study the column has been exposed to two different bending modes, depending on the FT- and the FC-series. Two different classifications are therefore needed. The calculations are presented in App. F.

The classification of the column's cross-section is based on the local slenderness and the stress distribution over the specific section. In addition is yielding of the material implemented by $\epsilon_{EC9} = \sqrt{250/\sigma_0}$. The compressional side of the profile is of interest since buckling only occurs in compression. Fig. 6.2 presents the different sections of the column that needs to be investigated. Section 1 and 2 is relevant for the FC-series, and section 3 and 4 decides the classification of the FT-series. The highest classifications will be the driving classification for the relevant series.

Section 4 displays a significant slenderness resulting in a class 4 cross-section. A column of class 4 is likely to retrieve a local buckling mode, which is expected

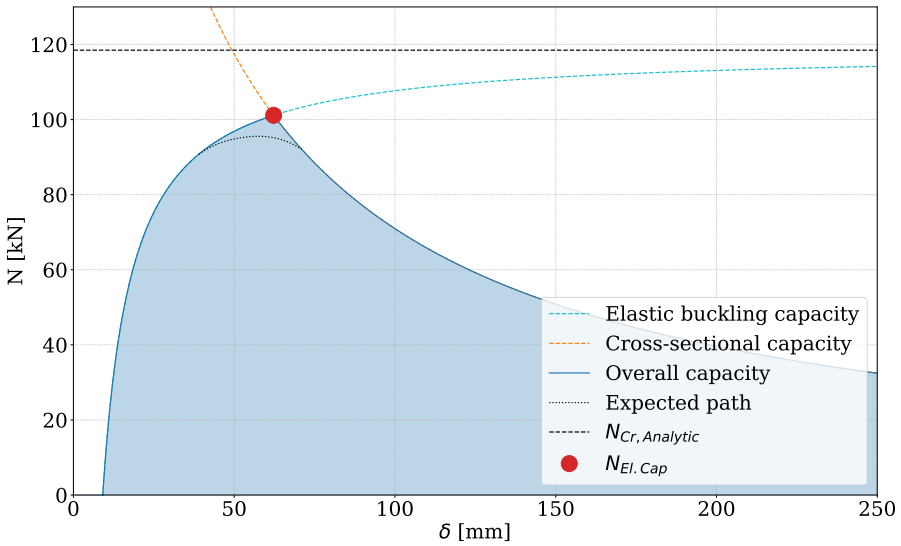

Figure 6.1: Definition of the buckling load in addition to illustration off expected path of the force-displacement curve.

to limit the capacity of the column. For the FC-series the cross-sectional class is reduced to 3. The cross-sectional class 3 is expected to undergo a global buckling propagation.

Table 6.1: Classification of the cross-section, EC9.

Description Description	Relevant series	β	β / ϵ_{EC9}	Class	Driving class
Sec. 1 (internal part) Sec. 2 (internal part)	FC	37.5 6.0	18.7 6.5	3 1,2	3
Sec. 3 (internal part) Sec. 4 (internal part)	FT	8.3 50.7	9.0 55.1	1,2 4	4

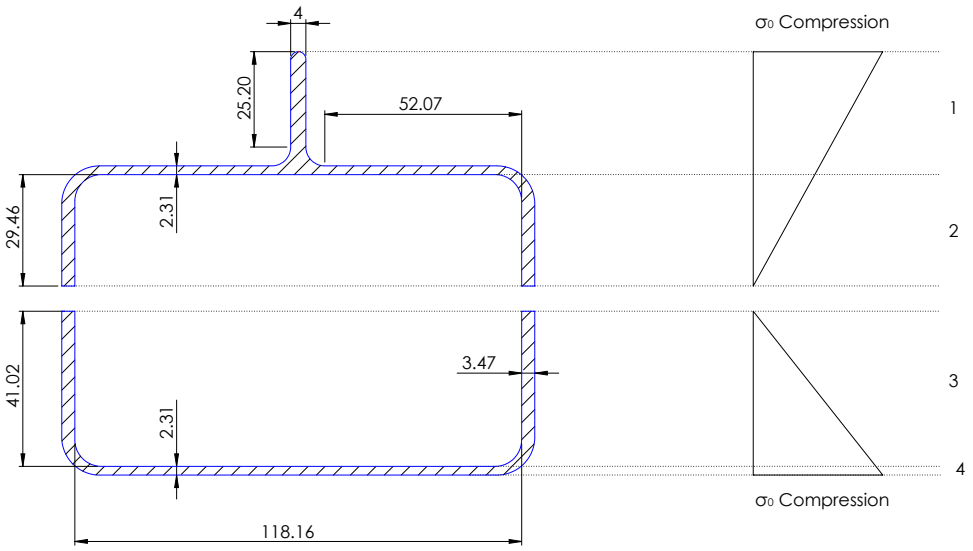

Figure 6.2: Division of the different sections regarding classification of the profile.

6.2 Theoretical approach

The elastic bending propagation is given as a function of axial load and basis on Euler's critical load, N_E, with initial deflection. These equations are presented in Ch. 2. Euler's critical load are calculated in App. F, found to be 118.5 kN. The cross-sectional capacity is, given in Ch. 2, is also given as a function of the axial loading and depends on the cross-sectional area and the elastic section modulus given in Tab. 5.1. These expressions are the comparison basis in the theoretical approach.

Considering the FC-series the bending propagation of the column corresponds well at the start of the elastic bending process, illustrated in Fig. 6.3. When the axial loading approaches the buckling load, the experimental data tend to rise above the theoretical values. The noticed ductility after the maximum axial load is applied, is remarkable. Exposing the flange to compressional stresses clearly contributes with a severe stiffness to the column. Since the cross-sectional capacity of the column is based on the yield stress of the material, it is possible to exceed the theoretical value. The material will exhibit strain hardening and contribute to high resistance post yielding. The yield stress could have been implemented as a function of the strains that occurred in the column, in an attempt to present the bending evolution more accurate. The elastic capacity tends to underestimate the FC-series, illustrated in Fig. 6.3. However, the elastic capacity load coincides well with the buckling load of the column. This indicates that the FC-series undergoes an elastic buckling propagation.

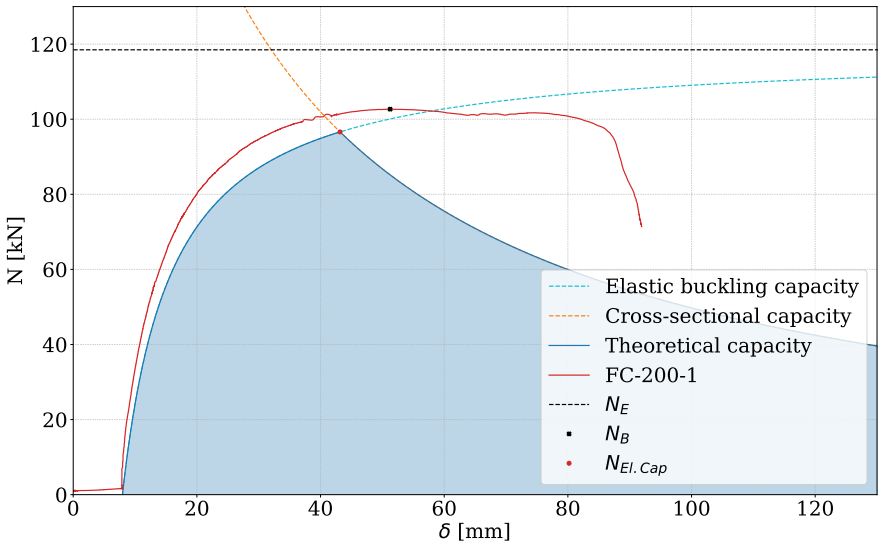

(a) FC-200-1.

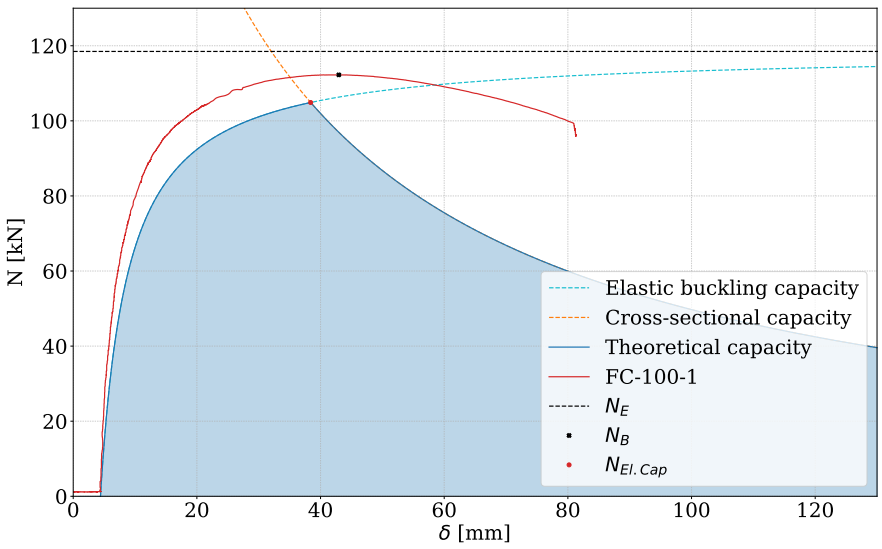

(b) FC-100-1.

Figure 6.3: Experimental tests compared against elastic buckling capacity and cross-sectional capacity for the FC-series.

One of the major weaknesses of the theoretical approach is that the cross-sectional slenderness of the column is not taken into account. I.e. that local buckling is not implemented as an alternative to failure. The FT-series illustrates the consequence of omitting this phenomenon in Fig. 6.4. The FT-series do decline prior to the elastic capacity load. As observed, the experimental data follows the elastic buckling propagation closely at the start of the process. It does, however, reach the buckling load at values far below the theoretical capacity, presented in Tab. 6.2. While observing the FT-series during the experimental testing, a local repetitive buckling pattern did occur just before the buckling load was reached. This buckling pattern can be observed in Fig. 5.6b in Ch. 5. The local buckling mode is a result of the cross-section reaching a bifurcation point of instability due to its high slenderness. This local buckling is fatal for the column and limits its capacity. This results in an overestimation of the buckling capacity as this theory is limited to secure elastic strains in the solution. Local buckling is however not implemented as a possible failure mode.

Table 6.2: Experimental data compared to theoretical solutions.

Description	N_B [kN]	$N_{El.Cap}$ [kN]	$\Delta N_{El.Cap}$ [kN]	$\Delta_{N_{El.Cap}}$ [%]
FT-200-1	83.0	94.3	11.3	13.6
FT-100-1	97.3	105.4	8.1	8.3
FC-200-1	102.7	96.6	-6.1	-5.9
FC-100-1	112.3	104.9	-7.4	-6.6

Tab. 6.2 presents the elastic capacity load and compares it to the buckling load of the column. The data presented in the table substantiate how the FC-series are underestimated, and that the FT-series are overestimated. It should be pointed out that the theory proposes a solution limited by an assumption that the strains will remain elastic. It is noteworthy that this approach does coincide well with the experimental tests. That is as long as they do remain either in the elastic regime or without local buckling, which the theory does not account for. The EC9 does, on the other hand, implement local buckling as an opportunity to failure.

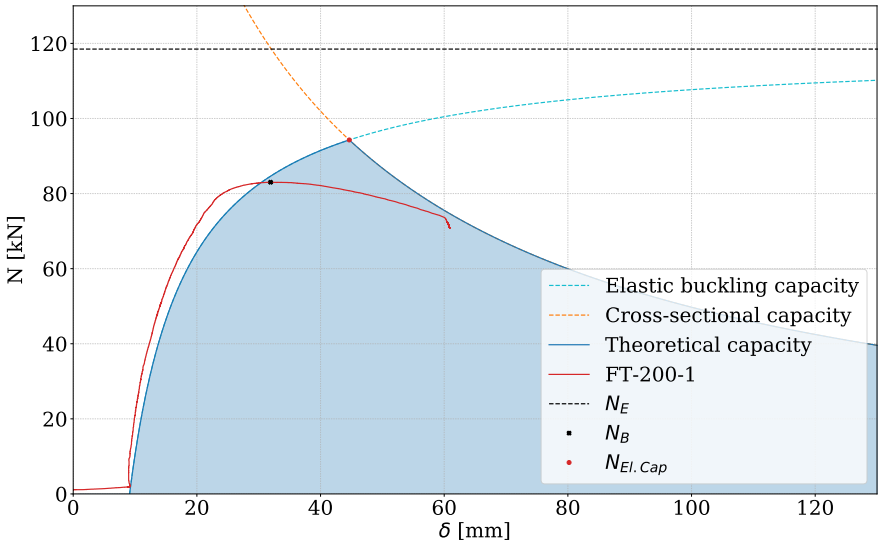

(a) FT-200-1.

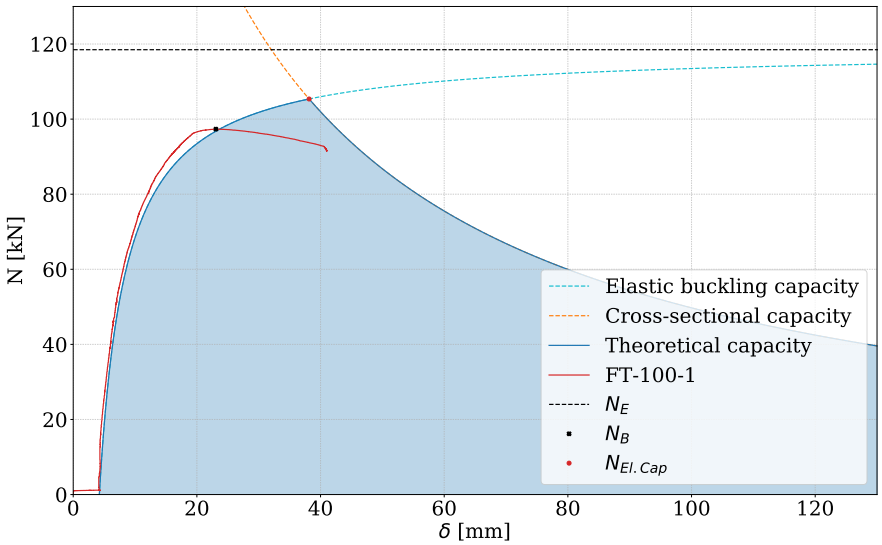

(b) FT-100-1.

Figure 6.4: Experimental tests compared against elastic buckling capacity and cross-sectional capacity for the FT-series.

6.3 Eurocode

The Eurocodes are a collection of advanced structural standards developed by an EU-collaboration in the purpose to ensure continuity and reliable constructions within the European Union [27]. These standards are by all means expected to retrieve a conservative recommendation of the capacity of load bearing members. A national annex is to be implemented into the Eurocode-calculations to that ensure that constructions remain within the national legislation. The safety factors is neglected in this study since the EC9 calculations are the topic of interest and the fact that these calculations are not to be used in a load bearing structure.

To calculate the critical load suggested by EC9 the Eq. 2.25 presented in Sec. 2.5 in Ch. 2 was utilized. There are five terms in this expression where two terms implement the weakening effects. That is κ due to welding, and a safety factor γ_1 defined in a national annex. They are both set to 1 in this calculation since the column does not obtain any welds and to approach the EC9 in a non-conservative manner.

The effective area (A_{eff}) is the key parameter that implements local buckling as an alternative to failure. For a cross-sectional class 1-3, the cross-sectional area will be considered as the gross area. This accounts for the FC-series presented in Tab. 6.1. This is due to a qualitative assumption that local buckling does not seem likely to appear in these sections. For a class 4, the area will be reduced, which accounts for the FT-series. The reduction of the area is applied to the class 4 section, which is the major side of the profile. This is done due to a prediction that this section will retrieve local buckling. The gross area and reduced area are stated in Tab. 6.1. An implication of reducing the area is that the neutral axis will be translated, and the elastic section modulus W_y will be reduced. The equations that are utilized in the order to establish the critical load $N_{b,Rd}$ and the buckling load $N_{b,Ed}$ are given in Sec. 2.5 in Ch. 2. Important parameters used in the calculations are given in Tab. 6.1. The complete calculations are presented in App. F.

Table 6.3: Parameters implemented in EC9.

Description	FC-series	FT-series
χ [kN]	0.300	0.335
A_{eff} $[mm^2]$	1153.1	1019.8
C_y [mm]	43.3	48.7
W_y $[mm^3]$	19726.8	17039.5
$N_{Cr,EC9}$ [kN]	102.3	100.7

The EC9 underestimates the capacity of the column, as expected. For the FC-series, the underestimation of the capacity of the column was in the range 20-25 %, presented in Tab. F.4. These series was classified as a class 3 cross-section, presented in Tab. 6.1. Which corresponds well with the assumptions that the column undergoes an elastic bending propagation.

By comparing the FT-series to EC9, the deviation was about 10-12 % underestimation. This problem was classified as a class 4, predicting local buckling. As discussed in Ch. 5, it was observed that the column did achieve local buckling prior the buckling load, this might have limited the columns capacity. The calculations of this series are more appropriate in its representation of the column than for the FC-series.

Table 6.4: Experimental data compared to solutions from Eurocode 9.

Description	$\Delta N_{B,Exp}$ [kN]	$N_{B,EC9}$ [kN]	$\Delta N_{B,EC9}$ [kN]	$\Delta N_{B,EC9}$ [%]
FT-200-1	83.0	73.5	-9.5	-11.4
FT-100-1	97.3	86.9	-10.4	-10.7
FC-200-1	102.7	78.6	-24.1	-23.5
FC-100-1	112.3	90.1	-22.2	-19.8

EC9 presents a severe conservative solution for the critical loading, $N_{b,Rd}$, of the column. By considering the critical load in Tab. 6.3, the reduction between the series is negligible. As discussed in Ch. 5 it is a trend that the precision of the test decrease with the transverse loading of the column. A hypothesis was therefore that if multiple tests of a column exposed only to axial compression, would achieve low precision. By exposing the column to transverse loading the precision will increase. The point is that EC9 seems to be highly conservative when calculating the critical load. This might be explained by the uncertainties of the outcome when exposing the column to axial compression, omitting to bend.

Another finding in Ch. 5 was that the precision within the FT-series was remarkably high. While the precision within the FC-series was lowered. I.e. columns that achieve local buckling do achieve high precision. It is therefore reasonable that EC9 does estimate the FT-series more accurate than the FC-series. This due to the phenomena, where local buckling of the column do achieve high precision, and are, therefore, safer to estimate.

An illustrative plot was made in the order to examine the effect of transverse loading, illustrated in Fig. 6.5 by use of Eq. 2.26 given in Ch. 2. The momentum is given as $FL_b/4$, which is the momentum produced by point load at the midspan on a simply supported column. Linear regression was conducted through the experimental data. It should be pointed out that this will only be an indication, and that more tests need to be conducted for varying loads to achieve a realistic more curve.

By observing the curves below a transverse load of 300 kg, these curves do occur as parallel. This implies that the underestimation, lies at the calculations of the critical buckling force, $N_{b,Rd}$, and not in the expression where bending is implemented.

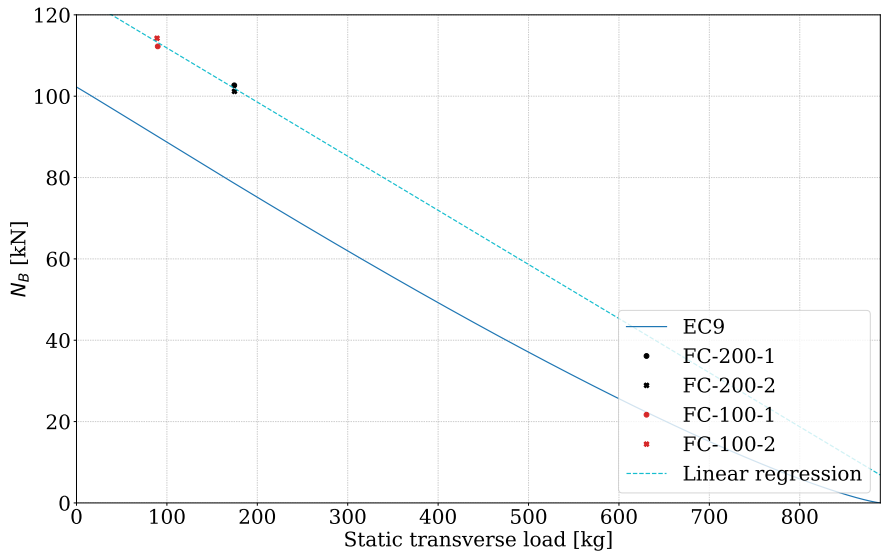

(a) FC-Series.

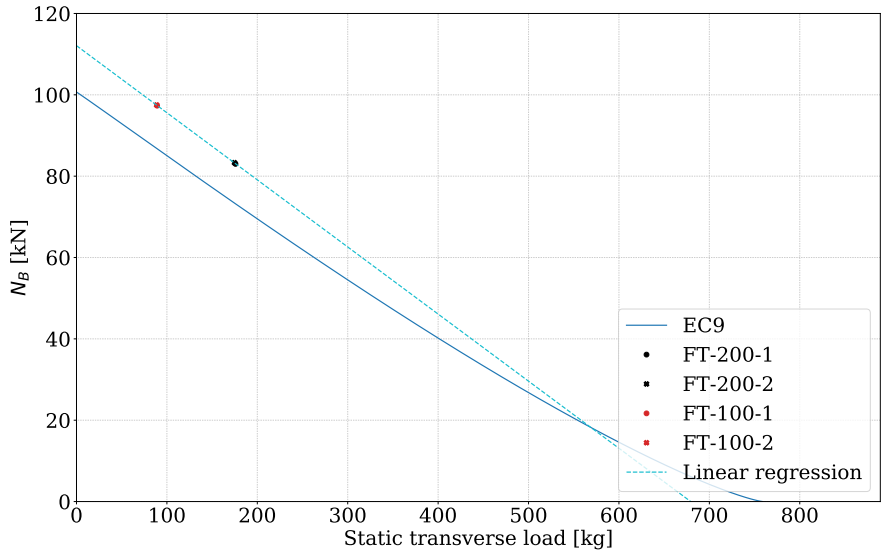

(b) FT-series.

Figure 6.5: $N_{B,Exp}$ plotted against EC9 with varying transverse load.

6.4 Interpretation

The theoretical approach contributes with very high precision as long as the column remains in the elastic region. However, the local buckling that occurs for the FT-series represents a phenomenon that this theory does not account for. For the FC-series it seems like the column obtains high plastic strains in exposed areas of the profile. This results in a remarkably high post-buckling ductility, which exceeds the elastic cross-sectional capacity.

For the solution calculated from EC9, the critical load, $N_{b,Rd}$, was found to be surprisingly conservative. Especially the FC-series achieved high deviations in the range of 20-25 %. The FT-series, on the other hand, estimated a less drastic solution in the range of 10-12 % underestimation. An explanation of the conservative solution of the critical load was the discussed. The instability that occurs as the column approaches its critical load makes it difficult to predict the outcome. EC9 calculates, therefore, a considerably large underestimation. In the experimental results, it was tendencies that the FT-series did achieve high precision. This can explain that EC9 implements a qualitative assumption based on that local buckling is easy to predict. Therefore, the buckling load can be calculated with less margin to the actual buckling load.

Another hypothesis is that EC9 overestimates the capacity of the column and that the high precision is caused by a weakness in the calculations. The critical load for the two series was estimated by EC9 to be more or less the same. However, by observing the experimental outcome it is clear that the FT-series achieves a significantly lower capacity than the FC-series. As the column holds a complex cross-section, it is reasonable to believe that EC9 struggles to predict the outcome. A conclusion can not be made, but this hypothesis could be interesting to examine in further work on the present topic.

To sum up this chapter the $N_{b,Rd}$, N_B and $N_{El.Cap}$ are presented in Tab. F.5. Both the analytical solutions underestimate FC-series. The FT-series resulted in a compromise between the two solutions.

Table 6.5: Critical axial loading from experimental testing and analytical calculations.

Description	FT-200-1 [kN]	FT-100-1 [kN]	FC-200-1 [kN]	FC-100-1 [kN]
$N_{El.Cap}$	94.3	105.4	96.6	104.9
N_B	83.0	97.3	102.7	112.3
$N_{b,Rd}$	73.5	86.9	78.6	90.1

Chapter 7

Numerical approach

The numerical analysis was established by utilizing the computer-aided engineering software Abaqus FEA. It is a is a powerful tool and absolutely crucial when a further design of the complete power pylon construction is to be made. This due to the high demands that, sat to establish a lightweight construction. The model is defined based on the statement that one mistake is easy to detect, however, two mistakes might disguise one another. The numerical model is, therefore, established in a compromise between simplicity and exact recreation.

Results from the numerical analysis have been compared to the experimental data. The FT-series turned out to be time-consuming. The results, despite this, coincided well with the experimental results. The FC-series was less time consuming, however, deviated somewhat from the experiment.

3D solid elements are time-consuming but more accurate than shell elements. It recreates the geometry in a sufficient manner and manages to recreate shear over the element thickness. When implementing a numerical model for a constructional analysis the CPU time does become of sever interest. A shell model was therefore settled. The implementations and the results are presented at the end of this chapter.

The modeling and analysis based on the Abaqus Analysis User's Guide [11], the work done by Bell [35], Vestrum [36], and Hopperstad and Børvik [37].

7.1 Numerical modeling

There was conducted 2 numerical models, that is one for each series. The model consists of an ideal case where the boundary conditions are friction free. In addition, are the top support firmly mounted and will not achieve any translation. The transverse weight is model as discrete parts tied to the model. The transverse mid-span load is implemented as the mean value of the two tests within each test series. The material is defined by a Young' s Modulus of 70000 MPa and the most conservative of the Voce hardening laws, presented in Ch. 3.

It will be reasonable to run implicit analysis due to the assumed small non-linearities for both buckling modes as this is a quasistatic problem with small plastic strains due to the high slenderness of the column. The implicit analysis does, however, include a convergence criterion that needs to be fulfilled. The meshing of the model must be fine enough to obtain small non-linearities over the elements, and the overall analysis must not produce high geometrical non-linearities. The positive aspects of running implicit analysis are the time-saving effect compared to explicit, heavy time-consuming analysis, that demands complex equation solving. Also, the energy balance remains due to the convergence criteria while running implicit analysis, this is not the case for explicit analysis [**iMechanics**, 11].

7.1.1 Geometry and material definition

The numerical model consists of one part made as a extruded 3D solid of length 2500 mm, where the cross-section is illustrated Fig. 7.1. The dimensions of the cross-section is presented in Fig. 5.1 in Ch. 5.

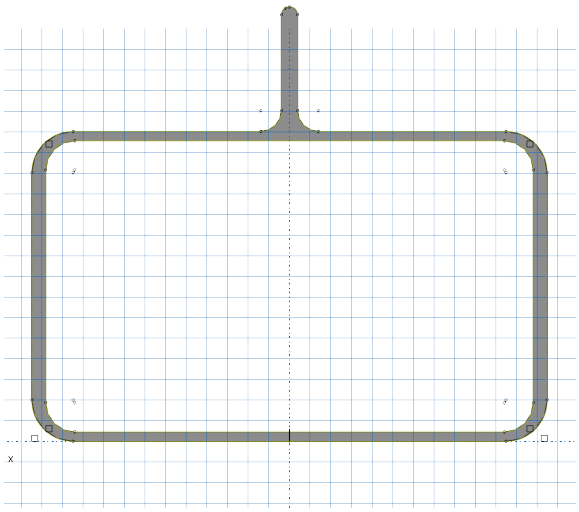

Figure 7.1: Modeling of cross section in Abaqus.

The material was defined in three steps. The first step defined the mass density of

the material. the second step defined the elastic behavior. These data are stated in Tab. 5.1. The third step defined the plastic behavior of the material. This was done by implementing an extrapolated Voce rule defined in Ch. 3.

Table 7.1: Profile specifications

Mass density	ρ	2700	kg/m^3
E-modulus	E	70 000	MPa
Poisson's ratio	ν	.33	-

7.1.2 Elements and meshing

The element selection was mainly denoted the quadratic 20 nodes, reduced integration. These elements are robust to non-linear deformations which are expected to occur in exposed areas in the column. In addition, do these elements appear as relatively friendly regarding computational time, compared with higher order elements. The FT-200 tests were, however, demanding while running the analysis and were therefore conducted with fully integrated elements which are time-consuming but did solve the problem of convergence that occurred. When it came to mesh sizing of the model, this was applied to a more empirical approach. It turned out that the FC-series did converge to a solution for a mesh size $5 \times 5 \times 5$ mm^3 , and that a mesh size of even as small as $2 \times 2 \times 2$ mm^3 did not give any significant improvement. For the FT-series a mesh size of $2 \times 2 \times 2$ mm^3 was needed to make the solution converge.

7.1.3 Boundary conditions and interactions

The supports were modeled by defining two reference points, below and above the component. They were located in the neutral axis of the cross-section of the column and at a distance of 85 mm. The reference points were attached to the node regions through a coupling interaction illustrated in Fig. 7.2a. The top support was free to rotate about the weak axis of the column. The bottom support was both free to rotate about the weak axis and translate in the axial direction. The axial load was applied to the reference underneath the column.

The transverse mid-span load was modeled in two different approaches for the FT- and the FC-series. The loading of the FT-series was modeled as a discrete rigid planar shell with dimensions that correspond to the strap that connected the transverse weight in the experiment, displayed in Fig. 7.3a. The discrete part was tied at the mid-span of the column. It was assigned a pressure that corresponds to the mean load measured at each test-series. For the FC-series the pressure was applied through a different part, illustrated in Fig. 7.3b. This separates the two models.

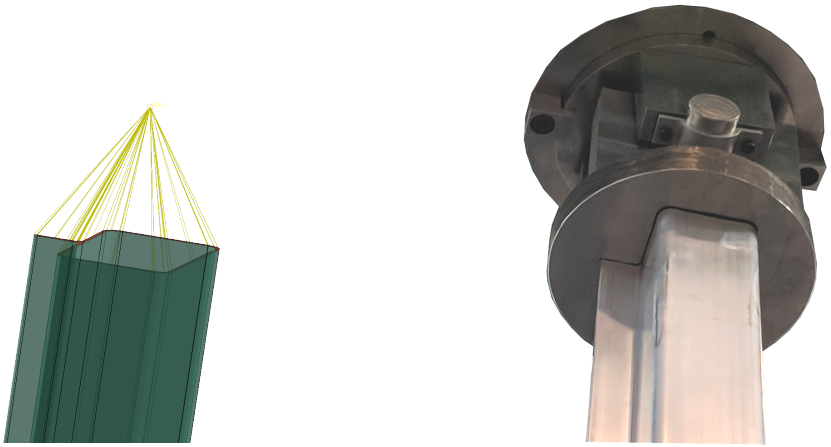

(a) Top support modeled in Abaqus. **(b)** Experimental setup of top support.

Figure 7.2: Designing model in Abaqus.

7.1.4 Steps

The loading of the column was applied in two steps. The first step makes sure that the transverse mid-span load was activated prior the axial compression was initiated. The transverse mid-span deflection was modeled as a pressure through the discrete rigid parts, that were tied to the column as in Fig. 7.3. The second step starts to load the column in axial compression. The load is applied in a displacement controlled manner, at the bottom reference point coupled to the component.

(a) Discrete part applied to the column for the FT-series. **(b)** Discrete part applied to the column for the FC-series.

Figure 7.3: Designing model in Abaqus.

7.1.5 Final model

The final model appears in its simplicity. A simplified description of the model follows.

The material is assigned in a non-conservative manner. There are not obtained any friction to the model as the supports used in the experimental setup are endeavored to appear as frictionless. This should lead the analysis in a conservative direction. When it comes to the transverse mid-span loading it was applied through a discrete rigid part, tied to the component. These parts can be assigned material properties so that they reproduce the strap or the wooden bricks used in the experiment. A friction interaction can be assigned to reproduce the interaction behavior more sufficiently. Friction interaction increases the complexity of the analysis. It was assumed that the discrete part was expected to occur with negligible stiffness, such that friction assignment was omitted. However, this implementation will make the column stiffer and lead the analysis in a non-conservative direction. These implementations do counteract with one another, either in a conservative or a non-conservative direction. This must be validated while running the numerical analysis since they have the characteristics to disguise one another. This can result in a numerical analysis that coincides with the experimental results, however in an incorrect manner. This will be discussed further in this chapter and in Ch. 8.

7.2 Numeric results

The numerical results for axial force and mid-span deflection are plotted in Fig. 7.4. The analysis was completed implicit which did result in a convergence problem for the FT-series. The time step decreased significantly when the analysis was approaching the buckling load. The convergence problem is therefore assumed to be caused by the local buckling pattern on the compression side of the column which led to high geometrical non-linearities. However, these series interacts with the experimental data in a convincing manner. The FC-series contributes to a more conservative solution when approaching the buckling load.

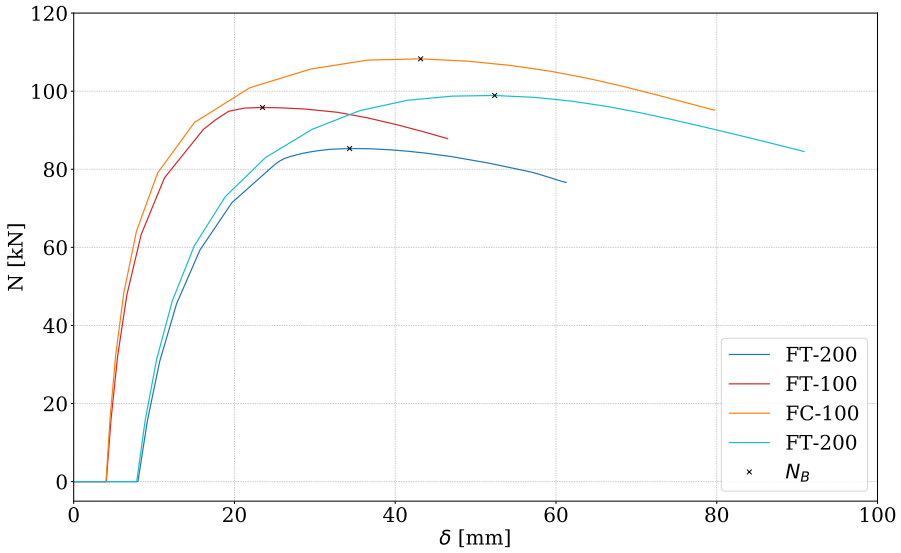

Figure 7.4: Experimental against numerical analysis, axial force and mid span displacement.

A practical consequence occurred by loading the column in two steps. One step for the transverse mid-span load, and one step for the axial load. The initial bending propagation deviates from the experimental results. The column was loaded with approximately 2 kN while completing the experimental test. To ensure that column did not slip out of its mounts. The loading process could have been applied in three steps in an attempt to reproduce the experiment in a more accurate manner. This is not expected to have any influence on the overall capacity, and was therefore omitted.

Tab. 7.3 presents deviations between the numerical analysis and the experimental tests, where the most distinct properties are highlighted. The FC-100 test stands out. At the most, the series underestimates the capacity of the column with 6 %. The FT-200 test overestimates the capacity of the column. It should be emphasized that the tabular values present the highest deviations encountered between the numerical model and the experimental data.

Table 7.2: Numeric analysis compared to experimental data. Maximum values within each series given.

Description Description	Δ_N [kN]	Δ_N [%]	Δ_δ [mm]	Δ_δ [%]	$\epsilon_{N,max}$ [-]	$\epsilon_{\delta,max}$ [-]
FT-200	-2.29	-2.8	-2.41	-7.6	0.022	0.032
FT-100	1.69	1.7	-0.45	-2.0	0.021	0.015
FC-200	3.78	3.7	-1.12	-2.2	**0.049**	0.089
FC-100	**5.97**	**6.0**	**-4.83**	**-12.6**	0.041	**0.105**

7.2.1 FT-series

From the experimental implementation in Ch. 5, it was found that the FT series undergoes a complex deformation process. Buckling first occurred local at the compressional side of the column, than globally. In addition, did the local buckling mode emerge as complex itself. It was a higher repetitive mode, and not an isolated local buckling. Due to this complexity, the FT-series turned out to be challenging numerically. There are two qualitative explanations for this problem. First, the high deflection, in addition to the local buckling pattern, contributed with high geometrical non-linearities. The analysis was completed implicit, and a convergence problem occurred due to these non-linearities. Secondly, buckling is an instability problem. An irregularity is essential to provoke its propagation. In the numerical model, this irregularity is absent, as the model is establish with the assignment of a perfect homogeneous material, and a geometry without any imperfections. The step time decrease drastically for the numerical model as the analysis do approach the buckling load. This is at a point where the local buckling pattern occurs. A model meshed with fully integrated solid elements with 20 nodes, at a size of $2 \times 2 \times 2mm^3$ made the solution converge. The local buckling pattern was reproduced in the numerical model, and is illustrated and compared to the experiment in Fig. 7.5.

Abaqus uses a Newton's method solver to encounter nonlinear equlibrium equations. The solution can obtain several thousand variables if the nonlinearities gets significant [38]. The CPU-time for the FT-series increase significantly while approaching the buckling load. As the solutions struggle to converge, the time steps decrease and the the Newtons method starts to call up on several variables to establish a solution. This is why the FC-series is time consuming.

A discrete part was tied to the column and applied pressure to recreate the transverse mid-span load. A consequence was that the tied section did not achieve any strains. This is revealed in Fig. 7.5a, dark, rectangular area indicates zero strains. This contributed to a false stiffness to the model. There was made an attempt to complete analysis where the transverse load was applied through a node section over the mid-span of the column. This analysis achieved in highly distorted elements at the node section, resulting in a convergence problem. Also, a frictional interaction between the discrete part and the column was conducted

whiteout achieving convergence. A study where the tying area was reduced was completed for the FC-series in an attempt to reveal the implication of assigning the transverse load in this manner.Further discussion on this topic will be presented in Sec. 7.2.2.

(a) Local buckling pattern from the numeric model.

(b) Local buckling pattern from the experimental test.

Figure 7.5: Local buckling that did occur shortly before the maximum axial load was applied the FT-series.

Despite the difficulties with the convergence, the FT-series results in an accurate solution. The modeled FT-100 tests successfully reproduced the experimental force-displacement development of the column, illustrated in Fig. 7.6. The buckling load, in addition, resulted to more or less the same displacement and axial loading as for the experiment.

When it comes to the FT-200 the solution overestimated the capacity of the column by a small percentage, presented in Tab. 7.3. This could be the implication of implementing the transverse mid-span load as a discrete rigid part. The rigid part opposes bending propagation of the column. The reason for this is that the column wishes to curve behind the discrete part, although is restricted by the tie interaction. Especially for large deflections of the column, as for the FT-200 series, this can have a considerable impact.

7.2.2 FC-series

The FC-series appears as an elastic global buckling problem as discussed in Ch. 5 and 6. A global buckling problem should be easier to analyze numerically. This assumption was enhanced by observing the numerical analysis where the CPU-time was significantly lower than for the FT-series. A reduction in CPU-time between the FT-200 and the FC-200 was about 95 %. It must be emphasized that the

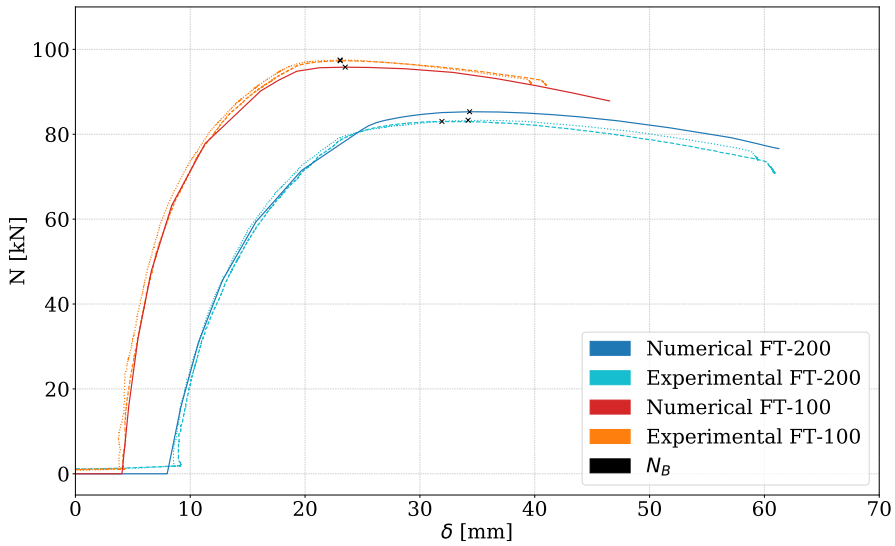

Figure 7.6: Experimental against numerical analysis for the FT series.

FT-200 analysis was submitted with fully reduced elements of size $2 \times 2 \times 2mm^3$, while the FC-200 contained reduced integrated elements of size $5 \times 5 \times 5mm^3$. That is 2 500 000 nodes against 400 000 nodes respectively.

The FC-100 analysis achieved its buckling load 6 % below the highest experimental test and at a displacement of 12 % off. Comparing to the experimental FC-100-1 test, the buckling load occurs at almost the same displacement, displayed in Fig. 7.7. The buckling load correlates in a more convincing manner. It should be pointed out that the experimental testing of the FC-100 tests achieved the lowest precision obtained. This can be an indication that the low accuracy of the numerical analysis is caused by a bad completion of the FC-100-2 test. The transverse load was applied as the mean value between the two FC-100 tests. However, this transverse load deviates with less than 0.1 %, and can therefore not explain this poor outcome.

The numerical analysis for the FC-200 tests underestimates the capacity of the column by a few percentages. The precision within this test series is high, and the buckling load occurred at more or less the same displacement as for the experiment, illustrated in Fig. 7.7. This affirms that the low coincidence within the numerical analysis and experimental FC-100 tests are due to bad precision within the experimental testing.

The flange of the column withstands high compressional stresses during the FC-series. In metals, a specimen can achieve a higher resistance while exposed to plastic strains in compression rather than tension. The material calibration in this study based on tensile tests alone, and cannot substantiate this assertion. Amundsen and Lynum have completed notch testes, both for tension and compression for

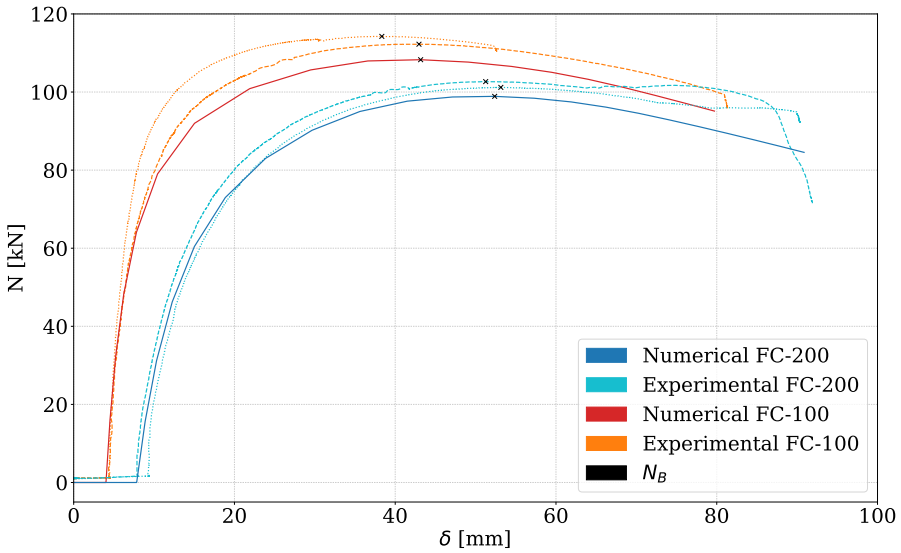

Figure 7.7: Experimental against numerical analysis for the FT series.

a 6082-T6 aluminium alloy [7]. Their Voce compression rule and tension rule are illustrated in Fig. 7.8. As observed is the hardening of the material found to be markedly higher for specimens exposed to compression rather than tension.

High compressional stresses will occur at the flange since the distance to the neutral axis of the column is significant, illustrated in Fig. 7.9. The neutral axis, at this stat, is denoted C_t, as this is a transitional neutral axis, somewhere in between the elastic neutral axis C_y and the plastic neutral axis C_p. The consequence of this distance is that a significant area of the flange will conceive yielding, while the tensional side of the cross-section still will remain in the elastic regime. If the material is to achieve a more strict hardening rule when exposed to compression rather than tension, this can explain why the FT-series reconstruct the experiment in a more accurate manner than the FC-series. Due to the fact that the compressional stresses for the FT-series will become fairly low compared to the tensional stresses at the flange. In addition, the FC-series achieved its buckling load at a higher displacement than the FT-series meaning that the stresses will become higher. This is validated in Tab. 7.3 where the strains for the FC-series becomes markedly higher than for the FT-series.

In an attempt to increase the capacity of the FC-100 series, the numerical model was assigned to Amundsen and Lynum's Voce hardening rule for compression. This occurred in a minor rise for the force-displacement curve for high displacement. However, first at the maximum axial load, which indicates that the plastic strains first become significant after the buckling load. This illustrates how the plastic contribution in this bending process is almost trivial. The maximum strains that occurred in the numerical model were for the FC-100 test, with a strain of approximately .1, presented in Tab. 7.3. However, these strains occur at the

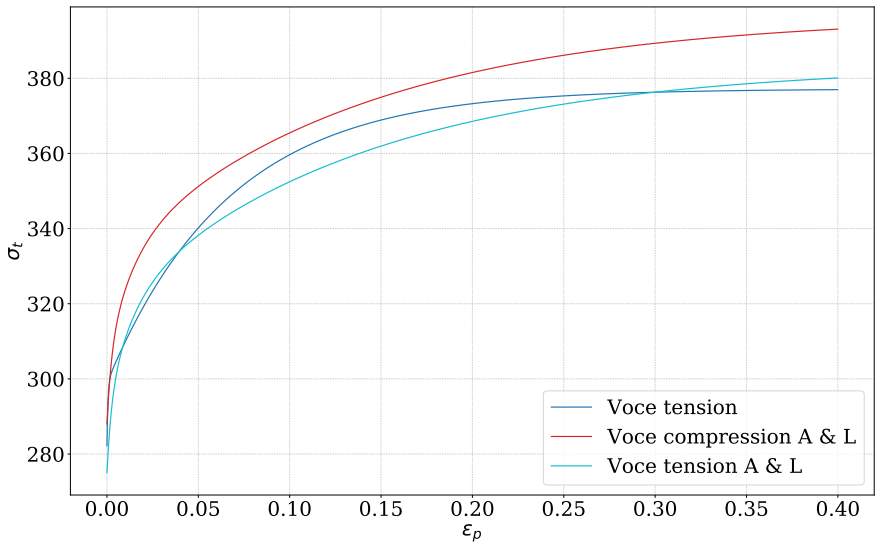

Figure 7.8: Amundsen and Lynum's material calibration for compression.

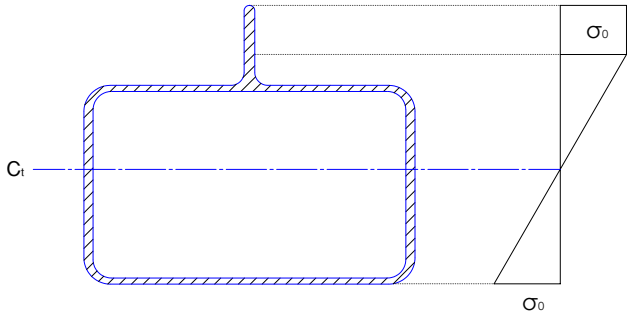

Figure 7.9: Strain distribution over the cross section.

maximum displacement the test was conducted to, which was significantly higher than the deflection the column retrieved while exposed to the buckling load. In addition, these strains were very localized and occurred around the discrete rigid part that is tied to the column, displayed in Fig. 7.10. This is not representative of the majority of the model and clarifies that the column remained elastic until the buckling load is applied.

Fig. 7.10 denotes that at the outermost of the flange, moderately high strains are presented. They occur both underneath and above the discrete rigid part, despite the fact that these strains are expected to occur at maximum deflection. These strains reveal the implication of tying the discrete part to the column. As the column tries to bend, the discrete part opposes the deflection, creating a momentum both above and underneath the part. This implies that this type of implementation of the transverse loading has its weaknesses and should be

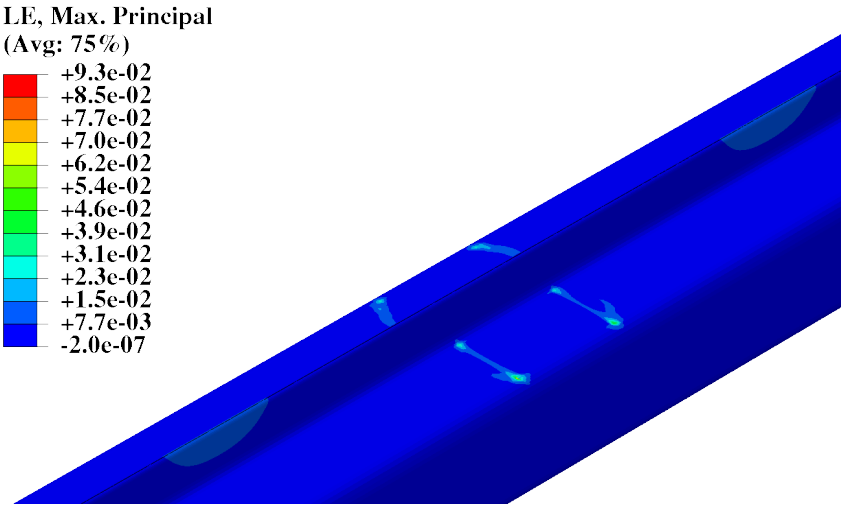

Figure 7.10: Illustration of the maximum strains that do occur for the FC-200 test.

improved in a further development of the numerical model.

In an attempt to detect the effect of the discrete rigid part, the area was reduced from a height of 75 mm to a height of 30 mm. This resulted in a decreased buckling load, displayed in Fig. 7.11. A reduction was expected as the discrete part was assumed to implement stiffness to the column. The buckling load decreased with approximately 2 %. The reduction of the discrete rigid art seems to have a small impact on the solution. To validate the implementation of the transverse load, it would have been interesting to implement friction interaction. This was not successful in this study but is recommended in eventual further work.

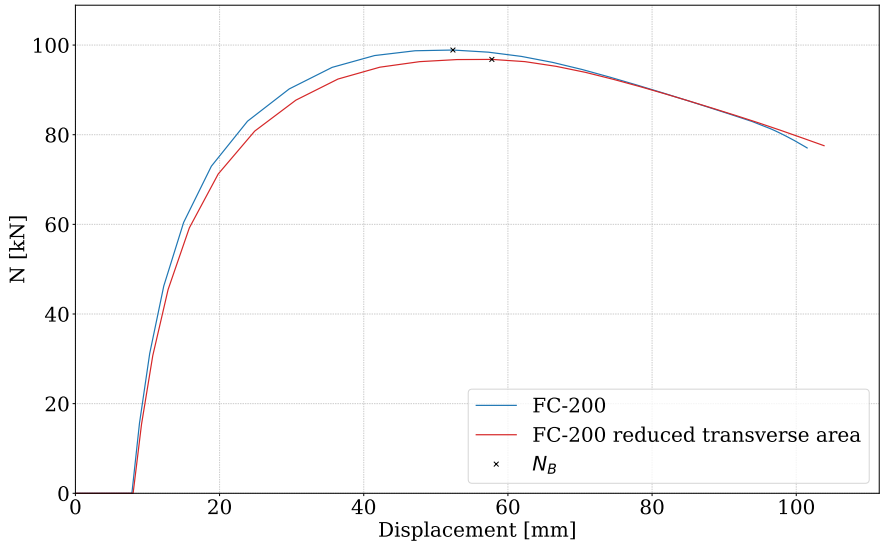

Figure 7.11: Implication of the reduction of the discrete rigid part.

7.3 Shell model

The shell model is implemented as a 3D deformable shell of type extrusion. The cross-section is constructed through the mean of the profile dimensions and assigned the relevant thickness for each section. The corners of the column are assigned the mean value of the corresponding sides. The final extruded model can be viewed in Fig. 7.12. The supports are modeled as a reference point tied to the top and bottom of the component as for the solid model. The transverse load was applied at the mid-span through a reference point, coupled to one transverse node-set over the column. The meshing of the model is conducted with 8 noded shell elements with a reduced integration of size 5×5 mm.

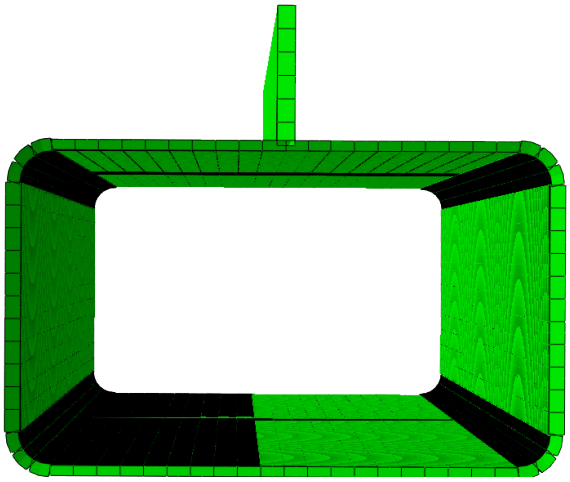

Figure 7.12: Modeling of cross section of the shell model in Abaqus.

The shell model was compared to the solid model for validation. The force-displacement curves are plotted in Fig. 7.13. The FC-series agrees with the solid analysis, however, underestimates the capacity by a few percentages. This can be a consequence of the assignment of transverse loading, as the shell model will not achieve the opposition against bending as the solid model. A better correlation occurs by comparing the FC-200 to the solid model with reduced discrete part. This implies that the shell model, in fact, does coincide in a convincing manner to the solid model. And that the deviation occurs due to the different methods of applying the transverse load. A shell model assigned a discrete part for transverse loading was not successful to obtain.

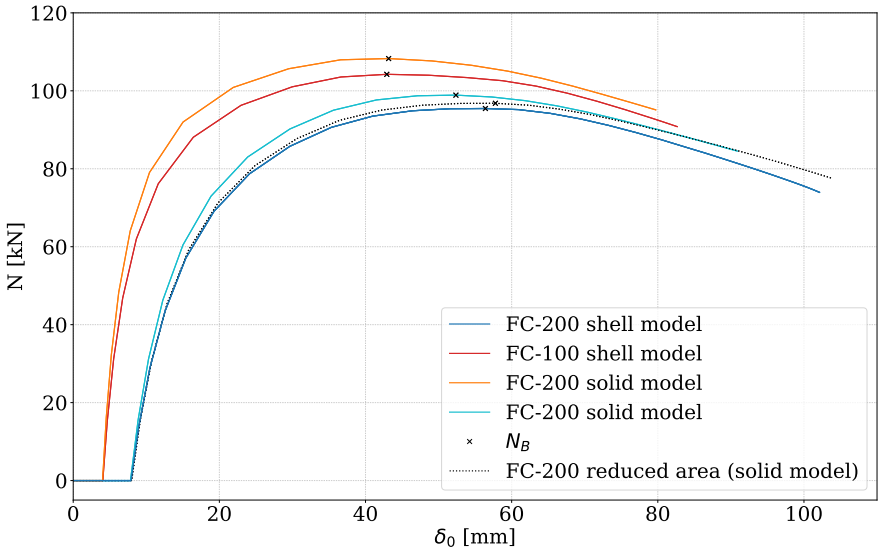

(a) FC-series.

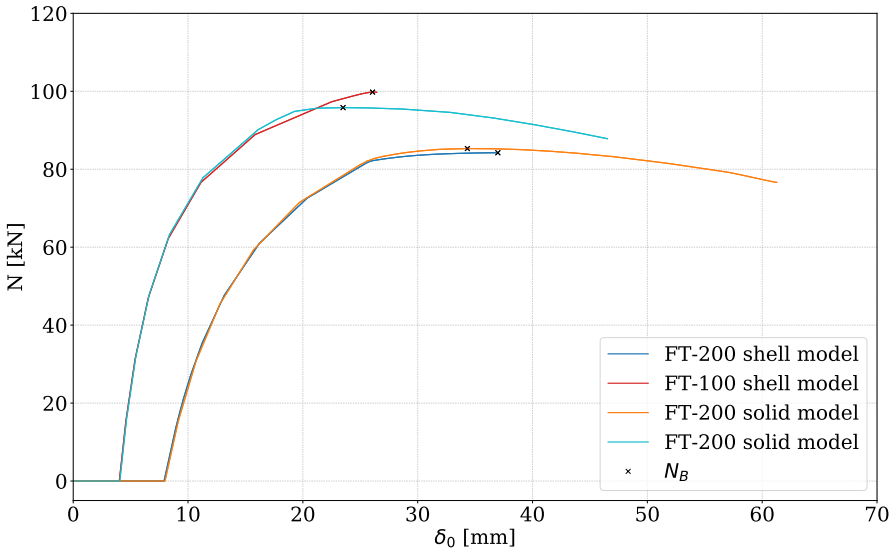

(b) FT-series.

Figure 7.13: Shell model compared to the solid model.

The FT-series does, as for the solid model, struggle to converge. Before reaching the buckling load, the shell model does, by far recreate the solid model. However, the time steps for convergence starts to decrease significantly, and the analysis does quit. This implies that the local buckling pattern is too complex to handle for the shell model. This can be a result of large shear forces that occur at the local buckling which the shell model does not manage to recreate [39].

The model was divided into four sections. That is the flange, the minor sides, the major sides and the corners. It was established a brief study on the effect of different thickness and length in the different sections of the shell model, presented in Fig. 7.14. By increasing the corner thickness to the major thickness of the side it corresponds to, a clear increase in capacity was observed. The flange was reduced by a length of two mm, since it does hold a round edge with a radius of two mm. The shell model represents a constant render thickness, illustrated in Fig. 7.12, so it could be interesting to look at this effect. A clear drop of the force-displacement plot occurred, which implies that the column is extremely sensitive to changes in the flange. This could be relevant to examine in a more comprehensive study.

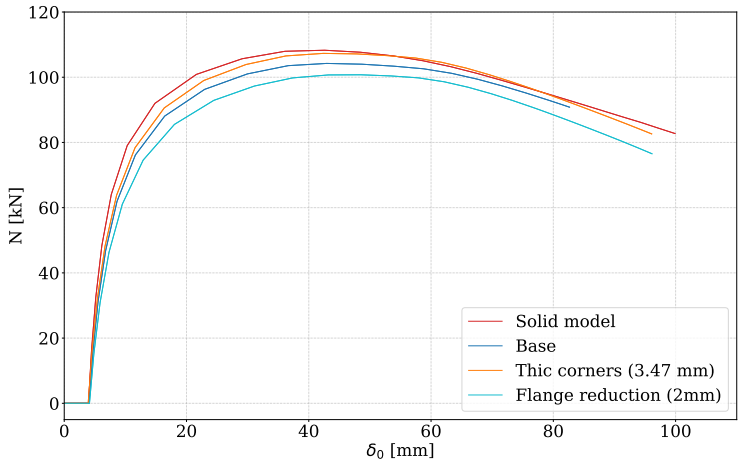

Figure 7.14: Study of the FC-100 shell model analysis.

7.3.1 Interpretation

By observing Fig. 7.6 and 7.7, the numerical model seems to coincide well to at least one of the experimental tests within each test-series. This is the case for the force-displacement propagation and coincidence to the buckling load. The precision between the numerical model and the best fit of the experimental test is as good as the precision within the experimental tests. The best fit between the experimental data and numerical model are stated in Tab. 7.3, and presents high precision.

Table 7.3: Numeric analysis compared to experimental data. Maximum values within each series given.

Description Description	Δ_N [kN]	Δ_N [%]	Δ_δ [mm]	Δ_δ [%]
FT-200	-2.00	-2.4	-0.13	-0.4
FT-100	1.52	1.6	-0.42	-1.8
FC-200	2.30	2.3	0.77	1.5
FC-100	3.97	3.5	-0.21	-0.5

A hypothesis for the underestimation of the FC-series was that the material could contain a more strict hardening law while exposed to tension rather than compression. The numerical model is assigned a material calibrated for tensile tests, which will coincide well for the FT-series since the major strains are expected to occur as tension in the flange. For the FT-series the major strains are also expected to occur in the flange, however, now in compression. If the material, in fact, exhibits a more strict hardening law while exposed to compressional stresses, this might have explained why the FC-series underestimates the experimental tests. However, it was found that by assigning a more strict hardening law to the material, the result was not affected prior buckling.

The least strict Voce hardening law was assigned to the material properties implemented in the numerical model. A possibility would have been to implement different material properties for the different sections the tensile tests was calibrated for. By assigning Amundsen and Lynum's hardening law calibrated for compressional material testing, it did not affect the results in any drastic manner. This implementation of material properties does, therefore, seem reasonable.

The convergence problem for the numerical model restricted the possibilities to conduct interesting parameter studies. This accounted for both the FT- and FC-series and became substantiated while running analysis of the shell model. Analysis with coupling interaction and friction between the discrete part and the column was not achieved. Since buckling is an instability problem, this can explain why a homogeneous material and geometry without imperfections are difficult to retrieve in a numerical analysis. By introducing a geometrical imperfection through a sinus variation in the longitudinal direction of the column, a hypothesis was that this would trig the local buckling modes and solve the convergence problem. This did

however not. In further studies, it could have been interesting to run the explicit analysis, especially in an attempt to better implement the transverse loading.

Chapter 8

Accuracy and precision

The precision in the experimental testing appeared high for the FT-series. The FC-series did achieve a higher divergence between the tests. This chapter will encompass a validation of the accuracy of the experiment, i.e. if the experiment measures what it was supposed to. In addition, will the precision of the numerical model be discussed. The translation and rotation of the supports, the transverse load, and the measurement techniques will be covered. The experiments were conceived in an attempt to test simply supported columns exposed to axial compression with a static transverse mid-span load.

8.1 Axial displacement

8.1.1 Supports

The bottom support was constructed to translate in the axial direction since the piston underneath is to apply an axial load to the column. The top support did not have the freedom to translate, and should stand still. There is some noise in the measurements, however, it is a distinct trend that the top support obtains low displacement in the axial direction. The top and bottom supports are plotted for all experimental tests in Fig. 8.1. The maximum displacement measured for the top support is 1.3 mm. This is 11.2% of the maximum bottom displacement. Compared to the total length of the column, of 2500 mm, this displacements are less than 0.1%, and should not affect the result in a drastic manner.

Validation of the numerical translation of the top support will not be a topic since this boundary was modeled as analytically rigid and will, by definition, only conceive rotation.

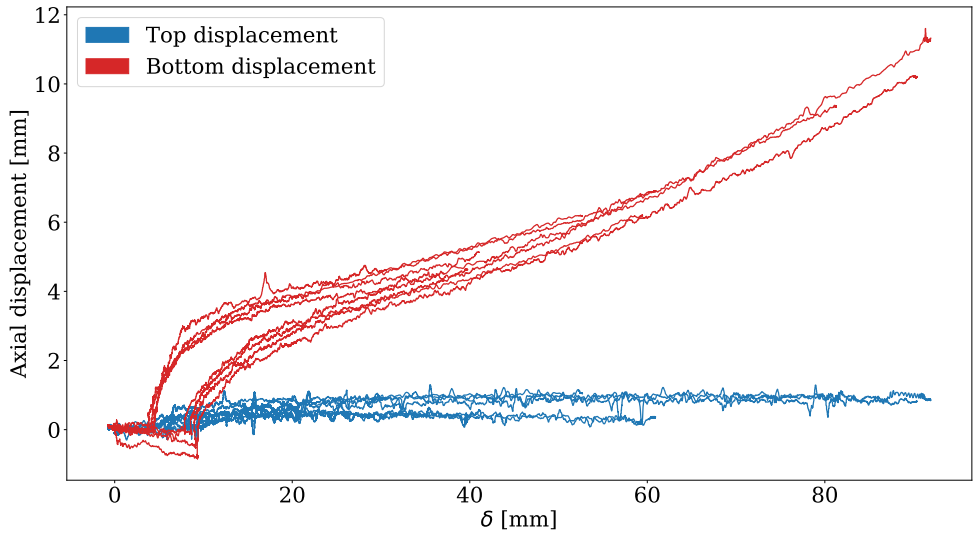

Figure 8.1: Axial displacement of the top against the bottom support.

8.1.2 Transverse measure

The laser that measures the transverse mid-span displacement of the column remains stationary while the column translated in the axial direction illustrated in Fig. 8.2. This implies that the horizontal displacement is measured at different points through the process. The maximum displacement of the bottom support is 11.6 mm. A conservative interpretation will be that the horizontal laser measured a point on the column that varied up to 11.6 mm. By assuming a sinus curvature, this will result in a horizontal displacement error of approx 0.32 mm. Maximum mid-span displacement measured was 90.72 mm. The error is then nearly 0.35%. I.e., the accuracy of the transverse measure remains high.

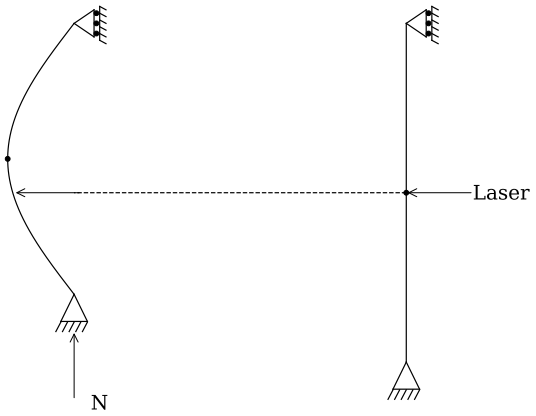

Figure 8.2

8.2 Rotation of supports

Another measurement that can be useful in an attempt to define the accuracy of the experiment is the rotation in both top (α_T) and bottom (α_B) supports. A simple supported model exposed to an axial load is expected to rotate simultaneously to the same extent. Some friction in the system can counteract the rotation and result in a bias of the rotation of the supports. Since a sinus function, where the rotation in the supports is a function of the deflection of the column, is assumed, rotation angles are expected to follow each other. There is some numerical noise in the measurements in Fig. 8.3, but it is a clear trend that the rotation in the supports follows each other.

The supports are modeled as frictionless in the numerical model. Linear regression of the experimental data of the top and bottom rotation of the supports are com-

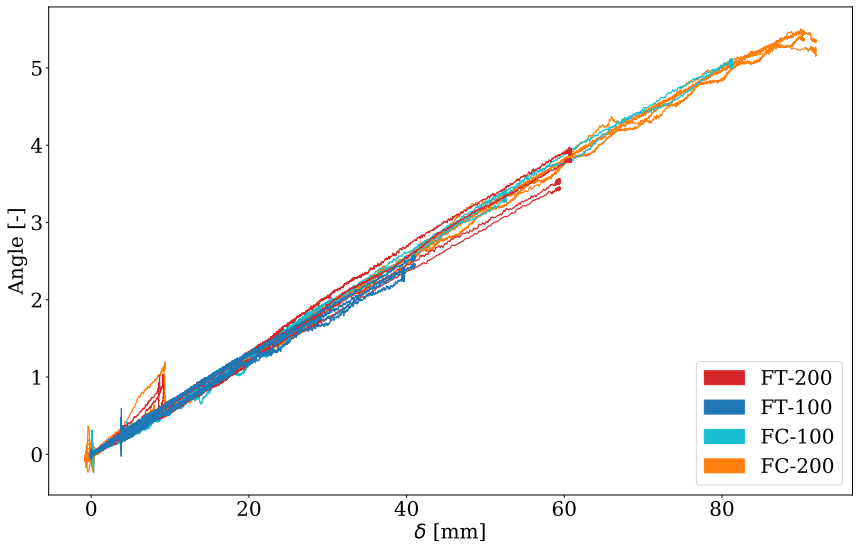

Figure 8.3: Experimental rotational data (α) for both top and bottom supports. Including all the experimental tests.

pared to the numerical analysis in Fig. 8.4. As observed there are small deviations between the experimental results for the top and bottom rotations. The numerical rotations are completely the same, as it is expected to be since column should operate without any geometrical or material defects. It appears as the rotation of the supports retrieved a high accuracy. However, there are some deviations regarding the precision, as the results from each test deviate somewhat from one another. To illustrate this contention the linear regression of the rotation of every test was extrapolated to a mid-span displacement of 100 mm. This resulted in a deviation of 13.1 % between the maximum and minimum rotation which occurred for the top rotation of the FT-200-1 and FC-200-1. The internal maximum deviation between the top and bottom rotation occurred for the FT-200-1 tests and was 3.8 %. This showed how the accuracy does occur as accurate since there are small deviations within the tests. However, the deviation between the test is a bit high, which insinuates low precision. It should be mentioned that this is a conservative method to interpret the rotational behavior of the supports, but it can be an indication that some phenomena in the experimental testing affect the results.

The deviation of the supports can also have been caused by human error as the transverse mid-span load was placed by hand. If the load were to be applied closer to one of the supports than the other the column would have conceived a larger rotation at the supports closest to the transverse load. However, this can explain bad precision and not low accuracy. Which is the same for a material defect or a geometrical defect which could cause the column to deflect unsymmetrical about the midpoint.

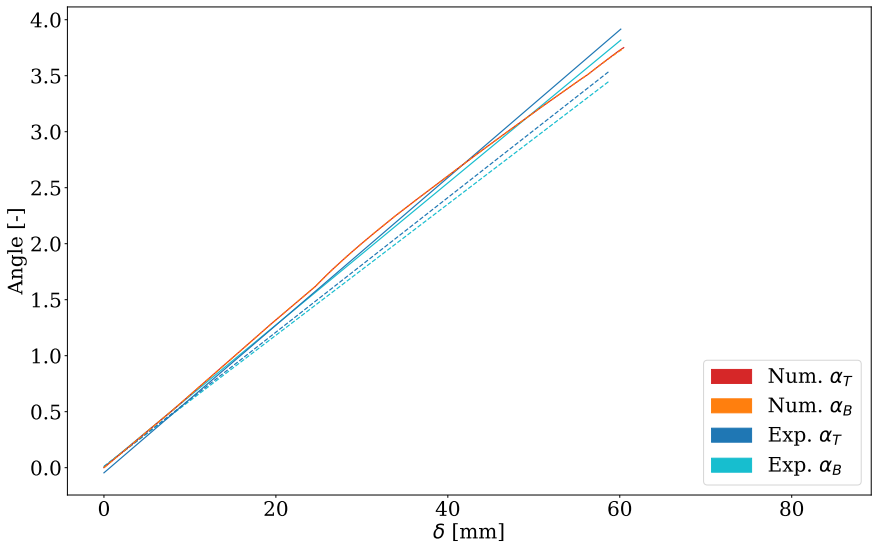

Figure 8.4: Linear regression of the rotation in the supports for the FT-200 test compared to the numeric approach.

One explanation for the accuracy can be that the frictional force in the supports increased as the axial loading of the column increased. The maximum deviation occurred between the FT-200-1 and the FC-200-1 where the axial load between these tests was approximately 20 % higher for the FC-series.

8.2.1 Implications of the numerical implementation

The numerical analysis was in a sufficient agreement to the experimental results. As discussed in Ch. 7. *Numerical approach* it is a trend that the precision between the numerical model and the best fit of the experimental test was as good as the precision within the experimental tests. A high coincidence with the experimental results does not necessarily mean that the numerical analysis reflects the experiment in a satisfying manner. As discussed in Ch. 7, there is the possibility that two bad implementations in a numerical model might mask one-another. The discrete rigid parts that were tied to the column to apply transverse loading, turned out to be less successful. The major disadvantage occurred for the FC-series where the part contributed to stiffness since it opposed bending of the column. As the discrete part was reduced, so that the stiffness decreased, the force-displacement curve was lowered. By implementing the transverse load more realistic, for example through a coupling interaction assigned friction, the column could have been free to move underneath the discrete part. This would result in an even more soft solution of the column, which would have underestimated the capacity even more. This does imply that the numerical analysis, despite achieving high precision, does produce a reduced accuracy as it does not recreate the column realistically.

Chapter 9

Conclusion

Laboratory work has been conducted with the purpose to examine the capacity of a specific aluminium column. The column has been simply supported at the boundaries, exposed to axial compression and a static transverse mid-span load. The column did hold a hollow, thin-walled rectangular cross-section, with a flange perpendicular to one of its major sides. The experimental tests have been conducted by bending the column about its weak axis, exposing the flange to both tensional and compressional stresses. The experimental values have been compared to both analytical solutions and numerical analysis.

Tensile tests were conducted to achieve material properties for implementation in a numerical model. And to detect different material properties at different parts of the cross-section. The raw data were analyzed through DIC and processed through python. A constitutive stress-strain relation was established for each section. The minor side of the cross-section did obtain the most strict hardening law, while the flange did contribute to the least strict law. An explanation for this was that the flange did achieve convectional cooling at both of its surfaces, reducing its participation hardening process.

When completing the laboratory testing, observations of the FT-series reveled a repetitive local buckling pattern, moments before buckling load occurred. The FC-series, on the other hand, did undergo what seemed to be an elastic global buckling mode. High precision for the FT-series was found, while the FC-series encountered a noticeable deviation within the test-series. Buckling is an instability problem, defined by a response that is significant compared to the applied load to the system. An interpretation was that if buckling occurs as a local mode, the response is assumed to be relatively small compared to a global buckling mode. This can explain why FT-series encountered a higher precision than the FC-series.

Comparison to the theoretical approach substantiated that the FC-series, by far, exhibited an elastic global buckling mode. Force-displacement graph illustrated how the FC-series correspond to the theoretical elastic bending propagation. Post-buckling these series achieved high ductility. For the FT-series, comparison re-

vealed that the capacity by far was limited by the local buckling these series exhibited.

EC9 calculations underestimated the buckling load in the range of 20-25 % and 10-12 % for the FC- and FT-series respectively. The FT-series was calculated as a class 4 cross-section i.e. likely to be limited by a local buckling mode. EC9 estimated the capacity of this series with high precision. The FC-series was categorized as a class 3 cross-section, where local buckling is not accounted for. The underestimation of these series was significantly high. EC9 seemed to lower the discrepancy for columns that are expected to undergo a local buckling mode. This coincided with the experimental tests were the precision was high for columns that encountered local buckling, which makes it easier to anticipate the outcome.

Numerical analysis of the experiment achieved high precision. By consider the best fit for each series, the largest deviation of the buckling load was 4 %. A general interpretation is that the laboratory setup produces high accuracy. This was substantiated by the numerical analysis which was modeled as an ideal case. However, corresponds well with the experimental data. The comparison basis in this thesis is therefore applicable for further studies.

Chapter 10

Further work

This study has focused on a specific column, where eight experimental tests were exposed to four different scenarios. High precision was found within the FT-series. The FC-series resulted in a greater variation. By conduct several tests within the same series, it can confirm or deny these findings, to better achieve a comparative basis. This would especially be of interest by comparison with EC9, where the FC-series was underestimated significantly while the FT-series coincide in a greater extent.

Further studies should include experimental testing of the column at different length and transverse loading. This to examine the FT-series correlation between column slenderness, and local slenderness and buckling. Also the flange's response on decreased column length, considering local buckling for the FC-series. A validation of the EC9's solution for members in bending and axial compression compared to experimental testing can be a topic. Where the comparison can be based on a larger amount of experimental data than this thesis occupies. This to better validate solution based on EC9 and the column response.

An improvement for the numerical model should be possible to establish, as weaknesses in the current model did occur. Especially the transverse loading does need a more realistic implementation. An explicit analysis is in general time consuming, however, due to the difficulties with convergence for the implicit analysis, it is a possibility that explicit analysis is preferable. These type of analysis generates great possibilities for a parametric study, however, must be handled with caution as convergence is not a criteria these analysis possess.

A hypothesis was that the EC9 overestimates the capacity of the FT-series. A detailed study that addresses this topic would be of severe interest.

Further would a comprehensive study based on shell models be relevant. This to achieve time efficient members, favorable in an extensive analysis that the complete power pylons represent.

References

[1] Statnett. *Om Statnett*. URL: http://www.statnett.no/Om-Statnett (visited on 02/25/2018).

[2] SINTEF. *AluMast*. URL: https://www.sintef.no/prosjekter/alumast (visited on 06/06/2018).

[3] Aluminium.org. *Aluminum alloys 101*. URL: //www.aluminum.org/resources/industry-standards/aluminum-alloys-101 (visited on 03/15/2018).

[4] S. Guddal. *Welding on power pylons in aluminium*. In: *MA Thesis, Norwegian University of Science and Technology* (2016).

[5] Standard. *Eurocode 9: Design of aluminium structures - Part 1-1: General structural rules*. In: *European Committee for Standardization (CEN)* (2009).

[6] A. V. Nesje and P. A. Nilsen. *Power pylons in aluminium*. In: *MA Thesis, Norwegian University of Science and Technology* (2016).

[7] N. Amundsen and A. Lynum. *Buckling of hollow aluminum columns*. In: *MA Thesis, Norwegian University of Science and Technology* (2017).

[8] O. S. Hopperstad M. Langseth and L. Hanssen. *Ultimate compressive strength of plate elements in aluminium: Correlation of finite element analyses and tests*. In: *Thin-Walled Structures* 29 (1997).

[9] O. S. Hpperstad A. H. Clausen and M. Langseth. *Stretch bending of aluminium extrusions for car bumpers*. In: *Journal of Materials Processing Technology* 102 (2000).

[10] F. Paulsen and T. Welo. *Cross-sectional deformations of rectangular hollow sections in bending*. In: *International Journal of Mechanical Sciences* 43 (2001).

[11] Dasault Systems. *Abaqus Analysis User's Documentation*. URL: http://130.149.89.49:2080/v2016/index.html (visited on 03/15/2018).

[12] Autodesk. *Robot Structural Analysis Professional User's Guide*. URL: https://knowledge.autodesk.com/support/robot-structural-analysis-products/learn-explore/caas/CloudHelp/cloudhelp/2018/ENU/RSAPRO-UsersGuide/files/GUID-4A734308-B2F3-4147-A310-BD47C48E9ED1-htm.html (visited on 05/06/2018).

[13] Egil Fagerholt. *eCorr v4.0 Documentation*. URL: http://www.ntnu.edu/kt/ecorr (visited on 05/06/2018).

[14] Gimp. *Gimp 2.10 GNU Image Manipulation Program*. URL: https://docs.gimp.org/2.10/nn/ (visited on 05/06/2018).

[15] Python.org. *Python 3.6.5 Documentation*. URL: https://docs.python.org/release/3.6.5/ (visited on 05/06/2018).

[16] Dassault Systems. *Solidworks Help*. URL: http://help.solidworks.com/2018/English/SolidWorks/sldworks/c_introduction_toplevel_topic.htm (visited on 05/06/2018).

[17] The Latex Project. *Latex Documentation*. URL: https://www.latex-project.org/help/documentation/ (visited on 05/02/2018).

[18] Anderson T.L. *Fractuer Mechanics, Fundamental and Applications*. Vol. 3. 2005.

[19] J. G. Kaufman. *Introduction to Aluminum Alloys and Tempers*. 2000.

[20] Bauser M. Sauer G. and Siegert K. *Extrusion*. ASM International, 2006.

[21] P. Garbacz T. Giesko and A. Mazurkiewicz. *Inspection method of aluminium extrution process*. In: *Archives of Civil and Mechanical Engineering* 15 (2015).

[22] O. S. Hopperstadt and T. Børvik. *Materials Mechanics - Part 1*. 2015.

[23] E. P. Robert R. D. Cook D. S. M. Michael and J. Witt. *Concepts and Applications of Fenite Element Analysis - Fourth Edition*. 2001.

[24] Larsen P. K. *Dimensjonering av stålkonstruksjoner*. 1990.

[25] Wikipedia.org. *Buckling*. URL: https://en.wikipedia.org/wiki/Buckling (visited on 05/10/2018).

[26] J. M. Gere and B. J. Goodno. *Mechanics of Materials*. Seventh Edition. Fagbokforlaget, 2009.

[27] *Eurocode 0 and Eurocode 1 - Collection of National Annexes (NA)*. In: *Standard Online AS* (2014).

[28] G. Rodrigues. *Defining Accuracy and Precision*. URL: https://www.qualitydigest.com/inside/fda-compliance-article/defining-accuracy-and-precision.html (visited on 02/05/2018).

[29] Aalco Metals Limited. *6082-T6-T651 Plate*. URL: http://www.aalco.co.uk/datasheets/Aluminium-Alloy_6082-T6~T651_148.ashx.

[30] *Instron 5982*. URL: http://fab.cba.mit.edu/content/tools/instron/M10-16250-EN(RevB)%205980%20System%20Support%20Manual.pdf (visited on 11/04/2018).

[31] DanteDynamics. *DIC - Digital Image Correlation*. URL: https://dentecdynamics.com/digital-image-correlation (visited on 06/06/2018).

[32] N. McCormick and j. Lord. *Digital Image Correlation*. In: *materialstoday* 13 (2010).

[33] E. Fagerholdt. *Digital Image Correlation (DIC)*. 2017.

[34] j. M. Cimbala and Y.A. Cengel. *Fluid mechanics Fundamentals and Applications*. Third Edition. McGraw-Hill Professional, 2013.

[35] K. Bell. *An engineering approach to finite element analysis of linear structural mechanics problems.* Fagbokforlaget, 2014.

[36] Ole Vestrum. *Abaqus at SIMLab. Abaqus FEA*. Lecture note. (Visited on 03/03/2018).

[37] O. S. Hopperstad and T. Børvik. *Impact Mechanics - Part 1. Modelling of plasticity and failure with explicit finite element method*. 2017.

[38] Dassult Systems. *Nonlinear solutions methodsin Abaqus/Standard*. URL: `http://130.149.89.49:2080/v2016/books/stm/default.htm`.

[39] A. J. Sadowski and J. M. Rotter. *Solid or shell finite elements to model thick cylindrical tubes and shells under global bending*. URL: `https://spiral.imperial.ac.uk/bitstream/10044/1/14245/5/Element%20study%20paper%20V13%20130313%20Full%20manuscript.pdf`.

Appendices

Appendix A

True stress - true strain

By assuming that the volume will remain constant during elongation the following relations can be obtained.

A.1 True stress

$$\sigma = \frac{F}{A} = \frac{FA_0}{AA_0} \tag{A.1}$$

$$\frac{A_0}{A} = \frac{L}{L_0} = \frac{L_0\Delta}{L_0} = 1 + \epsilon_e \tag{A.2}$$

$$\sigma = \frac{F}{A_0}(1 + \epsilon_e) = \sigma_e(1 + \epsilon_e) \tag{A.3}$$

A.2 True strain

$$\epsilon = \int_{L_0}^{L} \frac{dL}{L} = ln(\frac{L}{L_0}) = ln(\frac{L_0 + \Delta}{L_0}) \tag{A.4}$$

$$\epsilon = ln(1 + \epsilon_e) \tag{A.5}$$

Appendix B

Solution off differential equation

This derivation are from the book "Dimensjonering av stålkonstruksjoner" [24]. The homogeneous solution are given in Eq. B.1.

$$\omega_1 = C_1 sin(rx) + C_2 cos(rx) \tag{B.1}$$

The initial deflection of the column are expected to retrieve a sinus shape given in Eq. B.2. Further deflection ω_1 are expected to be on the form given in Eq. B.3.

$$\omega_0 = \delta_0 sin(\frac{\pi x}{L}) \tag{B.2}$$

$$\omega_1 = Asin(\frac{\pi x}{L}) \tag{B.3}$$

By inserting Eq. B.2 and B.3 into the differential Eq. 2.22 and solve for the parameter A, a solution for the total deflection can be obtained B.5.

$$A = \delta_0 \frac{N/N_E}{1 - N/N_E} \tag{B.4}$$

$$\omega = \omega_0 + \omega_1 = \delta_0 \frac{1}{1 - N/N_E} sin(\frac{\pi x}{L}) \tag{B.5}$$

By setting $x = \frac{L}{2}$ the expression for the initial deflections effect on the total deflection can be obtained as in Eq. B.6.

$$\delta = \delta_0 \frac{1}{1 - N/N_E} \tag{B.6}$$

Appendix C

Material calibration

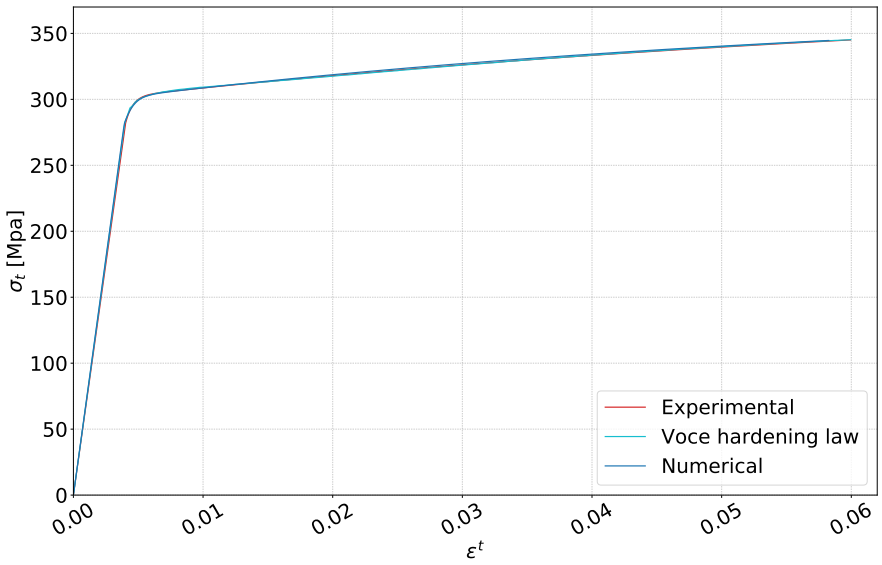

Figure C.1: The tensile test compared between numeric and experimental results for the AL-series.

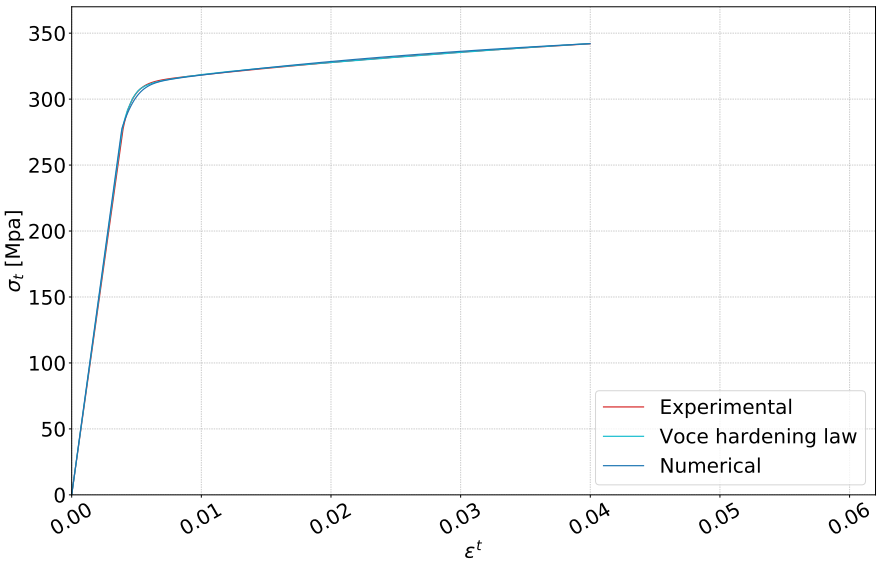

Figure C.2: The tensile test compared between numeric and experimental results for the AT-series.

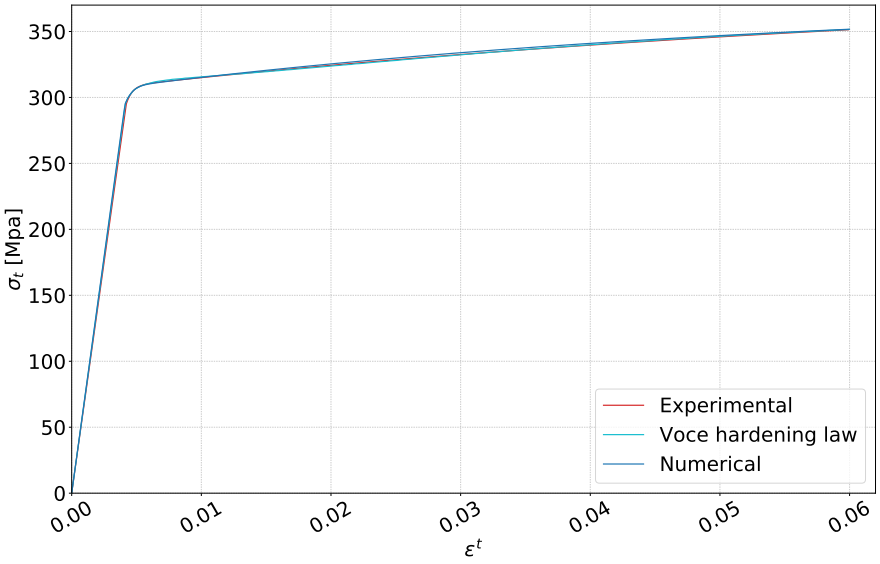

Figure C.3: The tensile test compared between numeric and experimental results for the BL-series.

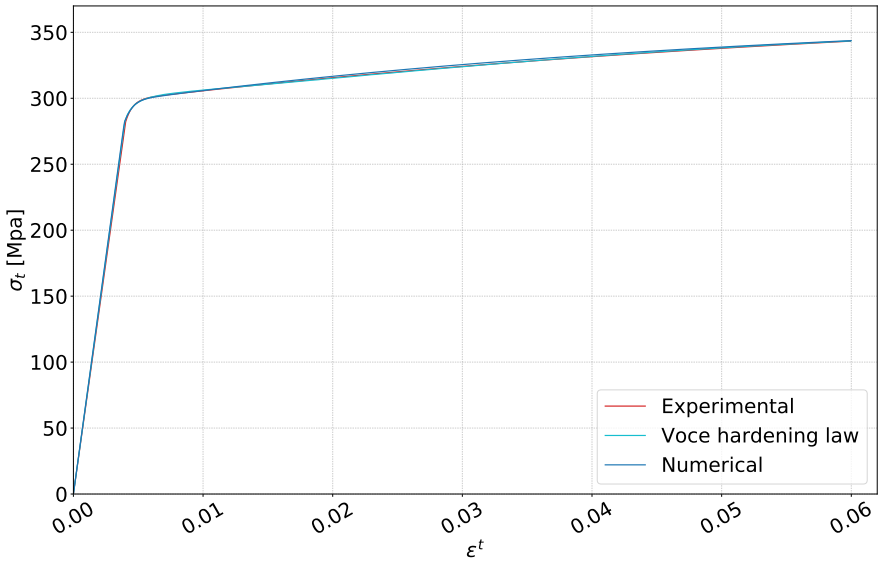

Figure C.4: The tensile test compared between numeric and experimental results for the CL-series.

Appendix D

Measurements

D.1 Tensile test

Table D.1: Dog bone measurement

Test	1	2	3
Test	$h \times w$	$h \times w$	$h \times w$
AL-1	4.99×2.32	4.99×2.32	4.99×2.32
AL-2	4.99×2.31	4.99×2.32	4.99×2.31
AL-3	4.99×2.31	4.99×2.31	4.99×2.32
AT-1	4.98×2.31	4.99×2.31	4.98×2.32
AT-2	4.99×2.32	4.99×2.31	4.99×2.31
AT-3	4.99×2.32	4.99×2.32	4.99×2.31
BL-1	4.99×3.48	4.99×3.48	4.99×3.48
BL-2	4.99×3.48	4.99×3.48	4.99×3.48
BL-3	4.99×3.48	4.99×3.48	4.99×3.48
CL-1	4.98×4.01	4.99×4.01	4.98×4.01
CL-2	4.99×4.01	4.99×4.01	4.99×4.02
CL-3	4.99×4.01	4.99×4.02	4.99×4.01

D.2 Experiment

Table D.2: Profile measurement

Test		A			B_1		B_2		C	
		1	2	3	1	2	1	2	1	2
FS-1	Topp	2.31	2.32	2.33	3.42	3.46	3.52	3.45	4.02	3.97
	Bunn	2.34	2.31	2.32	3.49	3.47	3.56	3.46	4.02	3.98
FS-2	Topp	2.32	2.31	2.29	3.47	3.46	3.47	3.44	4.02	3.98
	Bunn	2.29	2.31	2.33	3.48	3.49	3.49	3.46	4.02	3.98
FS-3	Topp	2.31	2.29	2.27	3.48	3.49	3.46	3.44	4.01	3.99
	Bunn	2.32	2.30	2.29	3.44	3.49	3.49	3.46	4.03	4.01
FS-4	Topp	2.35	2.32	2.30	3.48	3.50	3.46	3.46	4.03	4.00
	Bunn	2.29	2.32	2.37	3.49	3.48	3.52	3.47	4.05	4.03
FT-1	Topp	2.32	2.31	2.32	3.50	3.48	3.48	3.47	4.01	4.02
	Bunn	2.29	2.30	2.31	3.47	3.49	3.46	3.44	4.01	3.97
FT-2	Topp	2.32	2.29	2.27	3.43	3.51	3.44	3.47	3.96	4.02
	Bunn	2.30	2.31	2.31	3.47	3.45	3.51	3.44	4.03	4.01
FT-3	Topp	2.31	2.33	2.33	3.45	3.49	3.49	3.51	4.00	4.02
	Bunn	2.33	2.34	2.33	3.48	3.43	3.47	3.48	4.03	4.05
FT-3	Topp	2.30	2.30	2.31	3.47	3.48	3.47	3.45	4.01	4.01
	Bunn	2.33	2.33	2.32	3.49	3.46	3.44	3.46	4.01	4.02

Appendix E

Experiment

Table E.1: Testing abbreviations and order.

Description	State	Transverse load	Test nr.
FT-200-1	Flange in tension	200 kg	1
FT-200-2	Flange in tension	200 kg	2
FT-100-1	Flange in tension	100 kg	1
FT-100-2	Flange in tension	100 kg	2
FC-200-1	Flange in compression	200 kg	1
FC-200-2	Flange in compression	200 kg	2
FC-100-1	Flange in compression	100 kg	1
FC-100-2	Flange in compression	100 kg	2

Table E.2: Displacement in top and bottom supports.

Description	Bottom axial displacement [mm]	Top axial displacement [mm]	Differance [mm]	Differance [%]
FT-200-1	6.91	0.60	6.31	8.7
FT-200-2	6.20	0.82	5.38	13.2
FT-100-1	5.14	0.68	4.46	13.2
FT-100-2	4.64	1.08	3.56	23.3
FC-200-1	9.38	1.21	8.17	12.9
FC-200-2	6.20	1.22	4.98	19.7
FC-100-1	11.61	1.3	10.31	11.2
FC-100-2	10.23	1.29	8.94	12.3

Appendix F

Analytic calculations

F.1 Theoretical approach

The equations used to calculate the elastic bending propagation and the theoretical cross-sectional capacity are found in Ch. 2, and given below. As both the initial displacement and the cross-sectional capacity are functions of the axial load N, only the Euler's critical load are calculated and given in Tab. F.1.

Table F.1: Profile specifications

Cross sectional area	A	1153.1	mm^2
Neutral y-axis	σ_0	282.2	MPa
Neutral y-axis	C_y	43.3	mm
Neutral y-axis of 2. area of momentum	C_{0y} I^y	37.55 1222566.7	mm mm^4
Elastic section modulus	W_y	19726.8	mm^3
Euler's critical load	N_E	118.5	kN

Euler's critical load:

$$N_E = \frac{\pi^2 EI}{{L_B}^2} \tag{F.1}$$

Initial deflection:

$$\delta = \delta_0 \frac{1}{1 - N/N_{Cr}} \tag{F.2}$$

Cross-sectional capacity:

$$N(\frac{1}{A} + \frac{\delta}{W_y}) \leq \sigma_y \tag{F.3}$$

F.2 EC9

F.2.1 Classification

All calculations in this 'section are retrieved from *Eurocode 9: Design of aluminium structures - Part 1-1: General structural rules* [5]. They are therefore referred to for more comprehensive reading.

The stress distribution about the neutral axis are presented in Fig. F.1 as well as the different sections where slenderness of the cross section are to be evaluated.

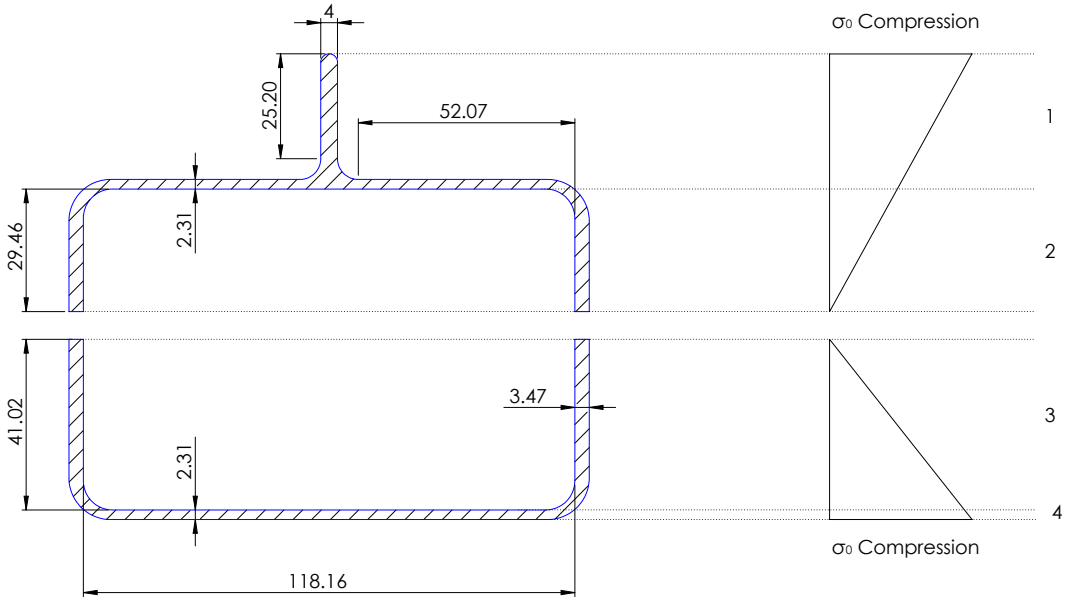

Figure F.1: Division of the different sections regarding classification of the profile. All measures in mm.

The classification of the cross section of the profile are based on the local slenderness and the stress distribution over the specific section. The compressional side of the profile are of interest since buckling only do occur in compression. Section 1-2 are therefore relevant for the FC-series and section 3-4 are relevant for the FT-series.

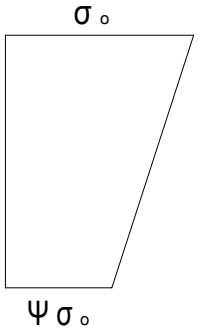

Figure F.2: Division of the different sections regarding classification of the profile.

$$\lambda_1 = \frac{118.16}{\frac{2.31+4}{2}} = 37.5$$

ht

$$\lambda_2 = \frac{29.46}{3.47} = 8.5 \qquad \psi_2 = 0$$

$$\lambda_3 = \frac{41.02}{3.47} = 11.8 \qquad \psi_3 = 0$$

$$\lambda_4 = \frac{118.16}{2.31} = 51.2 \qquad \psi_4 = \frac{41.02}{43.33} = 0.95$$

Slenderness of the different sections are defined by λ. The definition of χ is illustrated in Fig. F.2

$$\lambda = \frac{b}{t} \tag{F.4}$$

The strut in section 1 are a complex problem, such that the classification process differs from the other sections in the profile. The η parameter are calculated as in the following equation.

$$\eta = \frac{1}{\sqrt{1 + 2.5\frac{(c/t-1)^2}{b/t}}} \geqslant 0.5 \tag{F.5}$$

To classify this parameter are implemented as below, together with the η parameter.

t	b	c	η
$\frac{2.31+4}{2} = 3.155$	118.16	25.2	$0.49 \rightarrow 0.5$ (Restriction in Eq. F.5)

The remaining η parameters are calculated as follows:

$$\eta = 0.7 + 0.3\psi, \qquad (1 \leqslant \psi \leqslant -1) \tag{F.6}$$

$$\eta = 0.8/(1 - \psi), \qquad (\psi \geqslant -1) \tag{F.7}$$

Further are the β parameter implemented.

$$\beta = \eta \times \lambda \tag{F.8}$$

The ϵ_{EC9} parameter do implement the yielding of the material, presented in Eq. F.9.

$$\epsilon_{EC9} = \sqrt[2]{\frac{250}{\sigma_0}} \tag{F.9}$$

Where σ_0 is sat to 295.2 Mpa which was the largest yield point obtained from the material calibration. This to keep the calculation in non-conservative.

To classify the material the following relations are stated.

Parts in beams:

$\beta \leqslant \beta_1$: class 1
$\beta_1 < \beta \leqslant \beta_2$: class 2
$\beta_2 < \beta \leqslant \beta_3$: class 3
$\beta_3 < \beta$: class 4

Parts in struts:

$\beta \leqslant \beta_2$: class 1 or 2
$\beta_2 < \beta_2 \leqslant \beta_3$: class 3
$\beta_3 < \beta$: class 4

Material classification	Internal parts			Outstand parts		
	β_1/ϵ_{EC9}	β_2/ϵ_{EC9}	β_3/ϵ_{EC9}	β_1/ϵ_{EC9}	β_2/ϵ_{EC9}	β_3/ϵ_{EC9}
Class A	11	16	22	3	4.5	6

Table F.2: Classification of the cross sectional capacity regarding EC9.

Description Description	Relevant series	β	β / ϵ_{EC9}	Class	Driving class
Sec. 1 (internal part)	FC	37.5	18.7	3	
Sec. 2 (internal part)		6.0	6.5	1,2	3
Sec. 3 (internal part)	FT	8.3	9.0	1,2	4
Sec. 4 (internal part)		50.7	55.1	4	

F.2.2 Calculation

The FC series were classified as a class three and the area remains the same. For a class four cross section the area will be reduced to A_{eff}.

$$A_{eff} = (\rho_c tb)_{Class4} + A_{Residual} \tag{F.10}$$

$$\rho_c = \frac{C_1}{\beta/\epsilon_{EC9}} - \frac{C_2}{(\beta/\epsilon_{EC9})^2} \tag{F.11}$$

Where $C_1 = 32$ and $C_2 = 220$ for a Class A material resulting in $\rho_c = 0.51$.

$$\begin{aligned} A_{eff} &= 1154.14mm - 118.16mm \times 2.31mm + 0.51 \times 118.16mm \times 2.31mm \\ &= 1019.4mm^2 \end{aligned}$$

The implication of reducing the area is illustrated in Fig. F.3. Both neutral axis and elastic section modulus will change.

Figure F.3: Reduction of the class 4 area.

$$N_B = \kappa\chi A_{eff}\sigma_0/\gamma_{M1} \tag{F.12}$$

Where κ a parameter that includes weakening effects due to welds, which is sat to 1. γ_{M1} is a national annex safety factor sat to 1.

$$\chi = \frac{1}{\phi + \sqrt{\phi^2 - \overline{\lambda}^2}} \tag{F.13}$$

$$\phi = 0.5(1 + \alpha(\overline{\lambda}'\overline{\lambda}_0) + \overline{\lambda}^2 \tag{F.14}$$

$$\overline{\lambda} = \sqrt{\frac{A_{eff}\sigma_0}{N_E}} \tag{F.15}$$

Where N_E is the Euler's critical load of 118.5 Mpa. $\alpha = 0.2$ and $\overline{\lambda}_0 = 0.1$ due too material classification A.

Table F.3: Parameters of the critical loading regarding EC9.

Description	χ [-]	$A_{eff}[mm^2]$	σ_0 [Mpa]	N_B [kN]
FT-series	0.335	1019.4	195.2	100.7
FC-series	0.300	1153.1	195.2	102.3

F.2.3 Bending momentum

$$(\frac{N_{Ed}}{\omega_{0,EC9}N_{b,Rd}})^{1.3} + [\frac{1}{\omega_0}(\frac{M_{y,Ed}}{M_{y,Rd}})^{1.7})]^{0.6} \geqslant 1.0 \tag{F.16}$$

- $\omega_{0,EC9}$ is a factor that includes weakening effects due to welding and holes
- $M_{y,Rd}$ is the bending moment about the y-axis
- $M_{y,Rd}$ is the bending moment capacity about the y-axis

$\omega_{0,EC9}$	0
$M_{y,Rd}$	$\alpha_y W_{y,el} f_0$
$M_{y,Ed}$	$FL_b/4$
Class3	$\alpha_y = 1$
Class4	$\alpha_y = \frac{W_{y,eff}}{W_{y,el}}$
W_y	$19726.8mm^3$
W_y	$16837.8mm^3$

Table F.4: Experimental data compared to solutions from Eurocode 9.

Description	$\Delta N_{B,Exp}$ [kN]	$N_{B,EC9}$ [kN]	$\Delta N_{B,EC9}$ [kN]	$\Delta N_{B,EC9}$ [%]
FT-200-1	83.0	73.5	-9.5	-11.4
FT-100-1	97.3	86.9	-10.4	-10.7
FC-200-1	102.7	78.6	-24.1	-23.5
FC-100-1	112.3	90.1	-22.2	-19.8

Table F.5: Critical axial loading regarding EC9.

Description	FT-200-1 [kN]	FT-100-1 [kN]	FC-200-1 [kN]	FC-100-1 [kN]
$N_{El.Cap}$	101.1	109.1	102.9	109.5
N_B	83.0	97.3	102.7	112.3
$N_{b,Rd}$	73.5	86.9	78.6	90.1